The MOSDEF Survey

Accepted to ApJ
Preprint typeset using LaTeX style emulateapj v. 03/07/07

THE MOSDEF SURVEY: OPTICAL AGN DIAGNOSTICS AT $Z \sim 2.3$

Alison L. Coil[1], James Aird[2,6], Naveen Reddy[3], Alice E. Shapley[4], Mariska Kriek[5], Brian Siana[3], Bahram Mobasher[3], William R. Freeman[3], Sedona H. Price[5], Irene Shivaei[3]

Accepted to ApJ

ABSTRACT

We present results from the MOSFIRE Deep Evolution Field (MOSDEF) survey on rest-frame optical AGN identification and completeness at $z \sim 2.3$. With our sample of 50 galaxies and 10 X-ray and IR-selected AGN with measured Hβ, [O III], Hα, and [N II] emission lines, we investigate the location of AGN in the BPT, MEx (mass-excitation), and CEx (color-excitation) diagrams. We find that the BPT diagram works well to identify AGN at $z \sim 2.3$ and that the $z \sim 0$ AGN/star-forming galaxy classifications do not need to shift substantially at $z \sim 2.3$ to robustly separate these populations. However, the MEx diagram fails to identify all of the AGN identified in the BPT diagram, and the CEx diagram is substantially contaminated at high redshift. We further show that AGN samples selected using the BPT diagram have selection biases in terms of both host stellar mass and stellar population, in that AGN in low mass and/or high specific star formation rate galaxies are difficult to identify using the BPT diagram. These selection biases become increasingly severe at high redshift, such that optically-selected AGN samples at high redshift will necessarily be incomplete. We also find that the gas in the narrow-line region appears to be more enriched than gas in the host galaxy for at least some MOSDEF AGN. However, AGN at $z \sim 2$ are generally less enriched than local AGN with the same host stellar mass.

Subject headings: galaxies: high-redshift – galaxies: evolution – galaxies: active – galaxies: Seyfert

1. INTRODUCTION

It is now well established that the population of Active Galactic Nuclei (AGN), which trace the growth of supermassive black holes (SMBHs) via accretion, has evolved strongly with cosmic time (e.g., Boyle et al. 1993; Ueda et al. 2003; Barger et al. 2005). The overall accretion rate density peaks at a redshift of $z \sim 1-3$ (e.g., Hasinger et al. 2005; Ross et al. 2013; Ueda et al. 2014), similar to the overall star formation rate density (e.g., Boyle & Terlevich 1998; Silverman et al. 2008; Aird et al. 2010), indicating that the growth of galaxies via star formation and the growth of their central SMBHs via accretion are fundamentally linked.

This evolution of the AGN population is primarily driven by a rapid decline in the space density of the most luminous AGN between $z \sim 2$ and the present day, while the space density of lower luminosity AGN evolves more weakly and peaks at somewhat lower redshifts. This evolution is often described as "downsizing" and indicates that the most massive SMBHs likely undergo the bulk of their growth earlier in the history of the Universe than their lower mass counterparts (e.g., Ueda et al. 2003; Merloni 2004; Heckman et al. 2004). However, more recently it has also become clear that the overall fraction of galaxies hosting an AGN likely increases at higher redshift (e.g., Xue et al. 2010; Aird et al. 2013; Delvecchio et al. 2014), and thus AGN are more prevelent at earlier cosmic times. The physical details and extent of the co-evolution of galaxies and SMBHs during this key epoch when the bulk of SMBH and galaxy growth occurred remains unclear (e.g., Kriek et al. 2007; Hainline et al. 2012; Kocevski et al. 2012; Mullaney et al. 2012; Rosario et al. 2013; Jones et al. 2014).

It has been difficult to make progress on these questions in part because few low- to moderate-luminosity AGN have measursed spectroscopic redshifts at $z \gtrsim 1$, forcing most studies to rely on photometric redshifts (Xue et al. 2010; Brusa et al. 2010; Bongiorno et al. 2012). Furthermore, the lack of rest-frame optical spectra has prohibited many of the detailed studies of the relationship between host galaxy and AGN properties that have been performed at $z < 1$ (e.g., Kauffmann et al. 2003; Kauffmann & Heckman 2009; Hickox et al. 2009; Aird et al. 2012, among many others).

In order to determine the properties of AGN host galaxies at high redshift and to understand the physical drivers of AGN fueling and the co-evolution of galaxies and AGN, large spectroscopic surveys with well-understood selection effects are needed at $z \sim 1-3$, spaning the cosmic peak of AGN accretion. In particular, rest-frame optical spectra provide a wealth of information about the gas, stellar, and dust properties of galaxies, and while such information is now widely available at low redshift, it has until very recently been difficult to obtain at high redshift, due to the lack of multi-object near-infrared (NIR) spectrographs on 8-10m class telescopes.

In terms of identifying AGN within galaxy surveys, deep X-ray data provide unequivocal AGN identification as X-ray emission is a ubiquitous feature and identifies

[1] Center for Astrophysics and Space Sciences, Department of Physics, University of California, San Diego, 9500 Gilman Dr., La Jolla, CA 92093
[2] Department of Physics, Durham University, Durham DH1 3LE, UK
[3] Department of Physics and Astronomy, University of California, Riverside, 900 University Avenue, Riverside, CA 92521
[4] Department of Physics and Astronomy, University of California, Los Angeles, CA 90095
[5] Astronomy Department, University of California, Berkeley, CA 94720
[6] COFUND Junior Research Fellow

AGN that may be missed at UV, optical or IR wavelengths due to dust obscuration and/or host galaxy dilution. However, X-rays may fail to identify heavily obscured (Compton-thick) sources or lower accretion rate AGN (e.g., Gilli et al. 2007; Aird et al. 2012). Mid infrared (MIR) emission can also be used to identify AGN, where high energy radiation from the AGN is reprocessed by dust. Luminous AGN have a red power-law SED in the MIR, due to thermal emission from hot dust (e.g. Rieke & Lebofsky 1981; Elvis et al. 1994). Such MIR AGN selection can potentially also detect Compton-thick AGN that are missed by X-ray surveys (e.g. Donley et al. 2005; Alonso-Herrero et al. 2006; Polletta et al. 2006; Messias et al. 2012; Mendez et al. 2013). Thus, well-calibrated AGN identifications at different wavelengths are necessary to obtain a more complete AGN census.

At low redshifts, optical diagnostics such as the "BPT diagram" (Baldwin et al. 1981; Veilleux & Osterbrock 1987) have been widely used to identify AGN via the ratios of the nebular emission lines [O III] λ5008 to Hβ and [N II] λ6585 to Hα. This diagnostic can identify AGN in galaxies where the black hole is growing at a low rate and where the direct line-of-sight to the AGN is obscured. This diagnostic has been used to identify large numbers of AGN at $z < 0.2$ and has revolutionized our understanding of the demographics and physics of AGN at late cosmic times (e.g., Kauffmann et al. 2003; Heckman et al. 2004; Yan et al. 2006).

However, at higher redshifts these emission lines fall outside the wavelength coverage of optical spectrographs. In particular, at $z > 0.45$ the [N II] and Hα lines are redshifted to the observed NIR, and at $z > 1$ all four lines required for the BPT diagram are shifted to this wavelength. This has led authors to propose alternative optical AGN diagnostics using the [O III]/Hβ ratio and either rest-frame galaxy color (Yan et al. 2011) or stellar mass (Juneau et al. 2011). These diagnostics essentially use the known correlation between galaxy stellar mass and metallicity to replace the [N II]/Hα ratio with stellar mass or rest-frame color, which depends on stellar mass. These "color-excitation" (CEx) and "stellar mass-excitation" (MEx) optical diagnostics are calibrated using Sloan Digital Sky Survey (SDSS) sources in the BPT diagram at $z \sim 0.1$. The proposed AGN classification lines in the MEx and CEx diagram have been verified to $z \sim 0.8$ using deep X-ray data (Yan et al. 2011; Juneau et al. 2011). However, these diagnostics have been applied to galaxy samples at $z \sim 1-2$, assuming no evolution in the star-forming galaxy-AGN classifications (Yan et al. 2011; Juneau et al. 2011; Trump et al. 2011, 2013), until recently Newman et al. (2014); Juneau et al. (2014).

The BPT diagram in particular may require calibration at $z > 1$, as we know that galaxies at these redshifts are offset in this space towards the region of the diagram that contains AGN at $z \sim 0$ (Shapley et al. 2005; Erb et al. 2006; Liu et al. 2008; Yabe et al. 2012; Newman et al. 2014; Masters et al. 2014; Steidel et al. 2014). This known offset could be due to increased shock activity and/or different HII physical conditions (i.e., higher electron densities, temperatures, ionization parameters, N/O ratios) in high-redshift galaxies. If one assumes that the $z \sim 0$ BPT classifications of star-forming galaxies and AGN do not evolve, one could possibly infer an anomalously high AGN fraction at $z > 1$.

Using a sample of 36 galaxies and 4 X-ray sources in a flux-limited sample at $z \sim 1.5$, Trump et al. (2013) found that 2/3 of the galaxies in their sample may show evidence for an optically-selected AGN based on the $z < 1$ BPT, CEx, and MEx diagnostics, using the $z \sim 0$ classifications. Similarly, Juneau et al. (2013) infer for their 70 μm selected galaxy sample at $0.3 < z < 1.0$ a high AGN fraction (37%) that is twice that of previous similar studies, when they include optically-selected AGN identified using the MEx diagram that are not identified as AGN in either X-ray or IR emission. While these high fractions may result from evolution in the AGN fraction with redshift, they could also result from not allowing the $z \sim 0$ AGN classification lines to evolve with redshift. Several authors have also suggested that the observed offset of galaxies in the BPT diagram at $z \gtrsim 1$ could be due to contamination from weak AGN activity (Trump et al. 2011; Wright et al. 2010), though this would imply that almost all galaxies at high redshift harbor AGN, which seems unlikely.

It is clearly important to test AGN classifications in the BPT, MEx, and CEx diagrams at $z > 1$, to ensure that they these diagnostic diagrams can be used to robustly identify AGN, whether they are removed as contaminants from galaxy samples or studied in their own right. Estimates of the incidence of AGN activity at $z > 1$ in particular will be very sensitive to any evolution in the underlying demarcations separating star-forming galaxies and AGN in these optical diagnostic diagrams. Assuming no evolution could possibly lead to contamination of AGN populations by star-forming galaxies, while assuming more evolution than necessary could underestimate AGN samples.

Kewley et al. (2013a) recently published theoretical predictions for how the classification lines separating star-forming galaxies from AGN in the BPT diagram should evolve from $z = 0$ to $z = 3$, given different assumptions about ISM conditions in high-redshift galaxies, as well as the metallicities of AGN host galaxies. Kewley et al. (2013b) test the evolution in the star-forming galaxy/AGN classification in the BPT diagram using data from the literature to $z \sim 2.5$ and conclude that local calibrations should not be applied at $z > 1.5$. They derive a new redshift-dependent classification, which they test at $z \sim 2.5$ using a sample of 19 gravitationally-lensed galaxies. Juneau et al. (2014) also propose that the MEx classification should evolve with redshift and test evolution in both the BPT and MEx diagrams using samples at $z \sim 1.5 - 2$ from the literature. They find that while samples at $z \sim 1.5$ are large enough to study galaxy and AGN properties, at $z \sim 2$ the current samples are too small and have potentially strong selection biases.

Here we aim to test how well the $z \sim 0$ BPT, MEx, and CEx optical AGN diagnostics hold at $z \sim 2$, as well as test the new proposed evolution in the classifications separating star-forming galaxies and AGN in these diagnostics. Such tests require measurements of the success and contamination rate of AGN selection, where AGN have been unequivocally identified at non-optical wavelengths. To this end we use a statistical sample of NIR spectra from the MOSFIRE Deep Evolution Field (MOSDEF) survey, taken with the newly-commissioned MOS-

FIRE multi-object NIR spectrograph at Keck. We use measurements of the complete set of rest-frame optical emission lines required for the BPT diagram. We identify an unequivocal, *a priori* AGN sample based on X-ray and/or IR emission and use emission line ratios for galaxies and AGN in the MOSDEF survey to place $z \sim 2.3$ sources in the BPT diagram, as well as the CEx and MEx diagrams. As with all AGN selection methods, our *a priori* AGN sample is incomplete; however, it provides a reliable sample that is sufficient for the comparisons performed here. This methodology allows us to characterize the evolution of the division between star-forming galaxies and AGN in these optical diagnotic diagrams and discuss the completeness of optically-selected AGN compared to X-ray and IR-selected AGN at these redshifts.

The outline of the paper is as follows: §2 describes the data used here, including *Chandra* and *Spitzer* selection of AGN as well as our new MOSFIRE spectra. We additionally describe the methods used to measure emission line ratios, stellar masses, and rest-frame colors for our sources. In §3 we present our results and the location of MOSDEF galaxies and AGN in the BPT, MEx, and CEx diagrams. We discuss our results in §4 and conclude in §5. Throughout the paper we assume a cosmology with $\Omega_m = 0.3$, $\Omega_\Lambda = 0.7$, and $h = 0.7$.

2. DATA

We use spectroscopic data from the on-going MOSDEF survey (Kriek et al. 2014). This survey uses the recently commissioned MOSFIRE spectrograph (McLean et al. 2012) on the 10-m Keck I telescope. MOSFIRE is a multi-object NIR spectrograph that spans the wavelength range 0.97 μm to 2.45 μm and allows for the simultaneous observation of up to 46 individual sources over a $6' \times 3'$ field of view (we typically observe ~ 30 galaxies on a mask). The MOSDEF survey is being undertaken in three of the five CANDELS fields – COSMOS, GOODS-N, and EGS – in areas with coverage by the 3D-HST grism survey (Brammer et al. 2012) and when completed will produce moderate-resolution ($R \sim 3000$) rest-frame optical spectra for ∼1500 galaxies at $1.4 \leq z \leq 3.8$.

The full survey will use 47 Keck nights over the course of four years; here we use data from the first observing season, spanning December 2012 through May 2013. During this time a total of eight slitmasks were observed, including two slitmasks in the GOODS-S and UDS fields, which are not part of the main survey fields. The resulting sample at $1.4 \leq z \leq 3.8$ includes a total of 207 galaxies and AGN for which we obtained emission lines.

Targets for spectroscopy are selected down to fixed H-band (i.e., rest-frame optical) magnitude, using the *HST*/WFC3 F160W magnitudes provided by the 3D-HST team. We additionally use 3D-HST grism and photometric redshifts to increase the probability that targets will be at $1.37 \leq z \leq 3.8$ (Skelton et al. 2014). The MOSDEF survey targets sources in three specific redshift intervals ($1.37 \leq z \leq 1.70$, $2.09 \leq z \leq 2.61$, and $2.95 \leq z \leq 3.80$), such that the brightest rest-frame optical emission lines fall within atmospheric windows. We design slitmasks for a given redshift range, and each slitmask is observed in multiple filters to cover the entire rest-frame optical spectrum, including multiple emission lines from $\sim 3500 - 7000$Å. Here we focus on sources at $2.09 < z < 2.61$, which are observed in the J, H, and K bands. There are a total of 142 galaxies and AGN in this redshift interval in the MOSDEF data from the first observing season.

Target weights, which define the likelihood that a source will be selected as a spectroscopic target, are based on the *HST*/WFC3 F160W magnitude, with brighter sources given higher weights. The limiting magnitude for the $2.09 < z < 2.61$ sample is 24.5. Sources identified *a priori* as AGN using either X-ray or IRAC imaging data (details below) are given a higher targeting weight. Existing spectroscopic and photometric redshift information is also used in determining target weights, such that the MOSDEF sources are likely to fall in the redshift range of interest.

Slitmasks with sources at $2.09 < z < 2.61$ are observed for 2 hours in each of the J, H and K bands. Our $0.7''$slits result in resolutions of $R = 3300$, 3650, and 3600 in the J, H, and K bands, respectively. Masks were typically observed with an ABA'B' dither pattern, and seeing conditions were $\sim 0.5 - 1.0''$for most observations. The data were reduced with a custom IDL data reduction pipeline. Our spectroscopic success rate is extremely high; we detect emission lines for ∼85% of our targets. Details of the MOSDEF survey, target selection, data reduction, and galaxy sample characteristics are given in Kriek et al. (2014).

2.1. *X-ray AGN Identification*

AGN were identified prior to designing MOSDEF slitmasks using both *Chandra* and *Spitzer* imaging in our fields. In the COSMOS, GOODS-N, GOODS-S and EGS fields we identified X-ray sources based on the deep *Chandra* X-ray imaging. The depth of the *Chandra* data used in these fields is 160ks in COSMOS, 2Ms in GOODS-N, 4Ms in GOODS-S, and 800ks in EGS, corresponding to hard band (2-10keV) flux limits (over >10% of the area) of 1.8e-15, 2.8e-16, 1.6e-16 and 5.0e-16 erg/s/cm2 respectively. As the UDS currently lacks the deep, high-resolution *Chandra* data available in the other fields and is not one of the primary MOSDEF fields, we do not consider this field for our study.

The X-ray data from all the fields were reduced using a consistent procedure, as described in Laird et al. (2009, see also Georgakakis et al. 2014; Nandra et al. submitted). Point source detection was performed according to the method of Laird et al. (2009), applying a false probability threshold of $< 4 \times 10^{-6}$ (roughly corresponding to a $> 3\sigma$ detection) for sources in the full (0.5–2 keV), soft (0.5–2 keV), hard (2–7 keV) or ultra-hard (4–7 keV) energy bands. The source catalogs were merged to create a single multiband catalog in each field. We then identified secure multiwavelength counterparts to the X-ray sources using the likelihood ratio method (Ciliegi et al. 2003, 2005; Brusa et al. 2007; Luo et al. 2010), matching to sources detected at IRAC, near-infrared and optical wavelengths (see Nandra et al. in preparation for full details). These catalogs were then matched to the 3D-HST catalogs used for MOSDEF target selection, matching to the closest 3D-HST source within $1''$.

For X-ray sources observed by MOSDEF, we estimate 2–10 keV rest-frame X-ray luminosities for each source based on either the hard-band flux (when the source is detected) or the soft-band flux (otherwise).

TABLE 1
AGN Source Information

ID	Field	3D-HST ID[a]	RA	Dec	z	AGN identifier	log L_X (erg s^{-1})[b]
1	GOODS-S	42556	03:32:19.953	-27:42:43.152	2.30403	X-ray	43.56
2	GOODS-S	41886	03:32:23.436	-27:42:55.017	2.14214	X-ray	43.18
3	GOODS-S	41748	03:32:24.196	-27:42:57.551	2.30082	X-ray	43.30
4	COSMOS	10769	10:00:20.255	02:17:25.763	2.10321	X-ray	44.10
5	COSMOS	3146	10:00:31.820	02:12:43.542	2.10598	IR	<43.48
6	GOODS-N	22299	12:36:51.815	62:15:04.724	2.19391	X-ray	43.81
7	GOODS-N	14283	12:37:02.600	62:12:44.017	2.42009	X-ray	43.22
8	GOODS-N	21290	12:37:04.336	62:14:46.253	2.21490	IR	<42.88
9	GOODS-N	19082	12:37:07.189	62:14:08.090	2.48688	X-ray	43.51
10	GOODS-N	24192	12:37:23.188	62:15:38.425	2.24335	X-ray/ IR	43.69

[a] ID in 3D-HST v4.1 catalogs
[b] Rest-frame 2-10keV X-ray luminosities estimated from the counts in the observed 2-7keV (hard) band

We assume the X-ray spectrum is a simple power-law including only Galactic absorption with photon index $\Gamma = 1.9$. Our hard band flux detection limits approximately correspond to X-ray luminosity limits of $L_{2-10keV} \approx 1.3 - 15.1 \times 10^{42}$ erg/s at $z \sim 2.3$; sources at off-axis positions will have a higher detection limit. We note that at the redshifts probed by MOSDEF ($z > 1.4$) a relatively large absorption column ($N_H \gtrsim 10^{23}$ cm^{-2}) is required to significantly suppress the observed flux, even at 0.5–2 keV, so our luminosity estimates should be reasonably accurate, although a more sophisticated X-ray spectral analysis could indicate higher levels of intrinsic absorption and a higher X-ray luminosity.

For all galaxies in the MOSDEF sample that are not associated with an X-ray detection, we estimate upper limits on the X-ray luminosity. We extract the total counts from the X-ray images within a circular region corresponding to the 90% enclosed energy fraction (based on the *Chandra* PSF) for both the hard and soft bands. We estimate the background rate within the same aperture based on smoothed background maps and calculate the 95% highest posterior density confidence limit on the X-ray flux using the method of Kraft et al. (1991). We convert the upper limits on the hard and soft fluxes to X-ray luminosities using the same method as described above for the directly detected sources.

2.2. *IR AGN Identification*

As discussed above, deep X-ray surveys provide a highly reliable means of selecting AGN. However, at high column densities of $N_H \gtrsim 10^{23}$ cm^{-2} X-ray photons are absorbed, such that X-ray surveys can fail to identify the most heavily absorbed AGN. Such obscured AGN may instead be identified by their MIR emission, as high-energy radiation from an AGN is reprocessed by dust and re-radiated at MIR wavelengths.

Several selection techniques have been developed that use the unique colors of AGN in the MIR to identify infrared-AGN (IR-AGN) using data from the Infrared Array Camera (IRAC; Fazio et al. 2004) on *Spitzer* (i.e., Lacy et al. 2004; Stern et al. 2005). Here we select IR-AGN samples using the IRAC color criteria presented by Donley et al. (2012). This color-selection technique was designed to limit contamination by star-forming galaxies at least to $z = 3$ but still be both complete and reliable for the identification of luminous AGN. This was confirmed using large galaxy samples at intermediate redshift (Mendez et al. 2013), where it was shown that especially for deep IR surveys the Donley et al. (2012) selection criteria provides robust selection of AGN, free from galaxy contamination. Donley et al. (2012) compare their AGN selection criteria to various higher redshift samples at $z \sim 3$ and come to the same conclusion.

We use IRAC fluxes reported in the 3D-HST catalogs (Skelton et al. 2014). The IRAC 3.6, 4.5μm images in the main MOSDEF fields (AEGIS, COSMOS, GOODS-N) are from the Spitzer Extended Deep Survey (SEDS Ashby et al. 2013) v1.2 data release, while the 5.8 and 8μm images in AEGIS are from Barmby et al. (2008), in COSMOS from the S-COSMOS survey (Sanders et al. 2007), and in GOODS-N from the GOODS *Spitzer* second data release. Further details of the IRAC data are given in Skelton et al. (2014).

Following Donley et al. (2012), we require that objects are detected in all four IRAC bands, and have colors such that they lie within the following region in IRAC color–color space:

$$x = \log_{10}\left(\frac{f_{5.8\mu m}}{f_{3.6\mu m}}\right), \quad y = \log_{10}\left(\frac{f_{8.0\mu m}}{f_{4.5\mu m}}\right) \tag{1}$$

$$x \geq 0.08 \text{ and } y \geq 0.15 \tag{2}$$
$$y \geq (1.21 \times x) - 0.27 \tag{3}$$
$$y \leq (1.21 \times x) + 0.27 \tag{4}$$
$$f_{4.5\mu m} > f_{3.6\mu m} \text{ and } f_{5.8\mu m} > f_{4.5\mu m}, \text{ and} \tag{5}$$
$$f_{8.0\mu m} > f_{5.8\mu m}. \tag{6}$$

The AGN identified using these IRAC colors have some overlap with the X-ray-selected AGN. Generally, IR-AGN selection identifies more luminous AGN than X-ray selection (Mendez et al. 2013).

2.3. *Spectroscopic AGN Sample*

In our first observing season we targeted a total of 18 X-ray and/or IR-selected AGN, and we measured emission lines for 14 of these sources (the other four were likely outside of our observed redshift range). We emphasize that the fraction of the full MOSDEF sample that contains AGN should not be interpreted as the fraction of all galaxies at these redshifts that contain AGN, as AGN were given higher targeting weights when designing slitmasks.

Of the 14 AGN for which we obtained emission lines, here we present results for AGN at $2.09 < z < 2.61$ (this

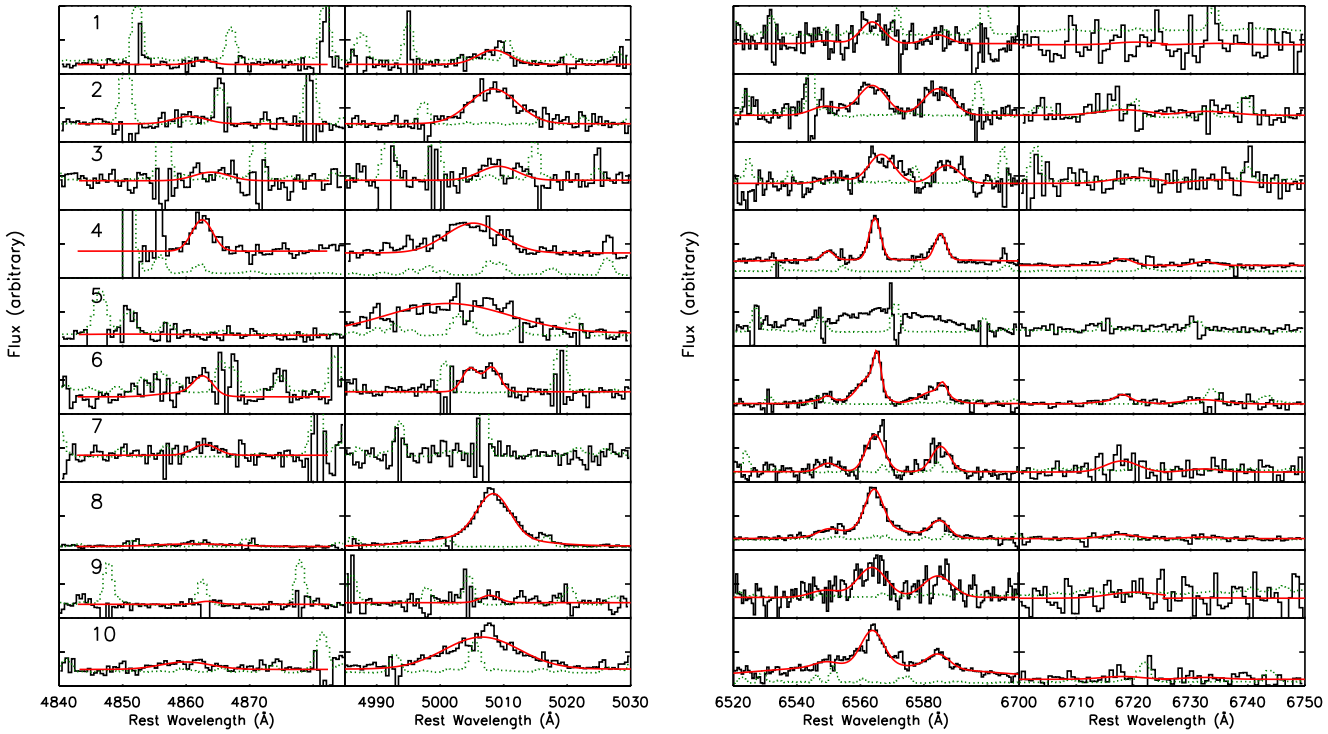

FIG. 1.— MOSDEF AGN spectra and fits for the Hβ, [O III], Hα, [N II], and [S II] emission lines. The observed spectra are shown in black, Gaussian fits in red, and error spectra with dotted green lines. The ID of each AGN is given in the upper left of the row. The y axis is scaled in the left panel to show the [O III] line well and in the right panel to show the Hα line well. Note that the wavelength width is not identical for each column; the third column with fits to Hα and [N II] has twice the wavelength range as the other columns. As discussed in the text, we do not fit Hα or [N II] for ID 5, due to the broad Hα emission, and for ID 7 we fit the [O III] λ4960 line instead of the [O III] λ5008 line, which is impacted by a night sky line.

excluded one AGN) and which had narrow emission lines and for which of the four lines used in the BPT diagram ([O III], Hβ, [N II], or Hα), at least either [O III] or Hβ *and* either [N II] or Hα were detected at greater than 3σ (this excluded three AGN). This criterion resulted in a sample of 10 AGN listed in Table 1. Two of these AGN were observed twice, on two different slitmasks; here we use the higher spectral S/N observation for each. As shown in Table 1, three of the ten AGN are identified as AGN using IRAC colors, and eight are identified as AGN using X-ray detections, with one AGN being both IR and X-ray selected. The log (L_X/(erg s^{-1})) values of our X-ray AGN are $\sim 43-44$; therefore these are moderate luminosity X-ray AGN. The mean redshift of the AGN sample is $z = 2.25$.

To measure line ratios, we fit Gaussian emission lines using the MPFIT non-linear least squares fitting function in IDL, where the error spectra are used to determine the errors on the fit. The fits are shown in Fig. 1. For the AGN presented here, we generally fit a single isolated Gaussian to Hβ, [O III] λ5008, [O I] λ6302, two Gaussians simultaneously to [S II] λ6718 and [S II] λ6733, and three Gaussians simultaneously to [N II] λ6550, Hα, [N II] λ6585. The deconvolved FWHM values (subtracting in quadrature the instrumental resolution) are $\sim 200-500$ km s^{-1}. For the three AGN with broad Hα emission where [N II] is still visible (IDs 4, 8, 10), we fit four Gaussians simultaneously to [N II] λ6550, Hα, [N II] λ6585, allowing for both a narrow and broad Hα component. The broad Hα components in these three AGN have FWHM values of $\gtrsim 1500$ km s^{-1}.

For AGN ID 8 we fit both a broad and narrow component to [O III] and Hβ, where the emission lines were not well fit by a single narrow component. In the BPT diagram we use the narrow components of each line, which have FWHM values of $\sim 200-400$ km s^{-1}, while the broad components have FWHM values of ~ 1100 km s^{-1}. For AGN ID 6, we fit two Gaussians to each Hβ, [O III], [O I], and [S II] line and six Gaussians simultaneously to [N II] λ6550, Hα, [N II] λ6585, allowing two Gaussians for each line. The FWHM values of each Gaussian are $\sim 100-500$ km s^{-1}. As we discuss further below, since both components are narrow we keep both in our sample here. We do not fit [N II] and Hα for AGN 5, where a very broad Hα line renders the [N II] line invisible. This AGN is therefore included in diagnostics that use only [O III]/Hβ but not [N II]/Hα. The FWHM of [O III] is 1370 km s^{-1}; we note that given the broad width of this line the [O III]/Hβ value on optical AGN diagnostics should be treated with caution. For ID 7 we fit the [O III] λ4960 line and scale the resulting flux and error by a factor of three to estimate the parameters for the [O III] λ5008 line, which is impacted by a night sky line.

In performing the Gaussian fits, we allow as much freedom as the data permit. We do not allow for a continuum slope local to the emission line, but we do fit for a flat continuum. We allow some freedom in the wavelength of the line center (up to 0.15%), though we fix the spacing between the S II and N II lines. We generally do not tie the widths of the different lines together for a single source, though we do require that the S II and N II lines have the same width of Hα. We force the [N II] λ6550 flux to be one third of the [N II] λ6585 flux, and we set a minimum width for the velocity dispersion of 1.5 Å in the

TABLE 2
AGN MOSDEF Derived Parameters

ID	log ([O III]/Hβ)	log ([N II]/Hα)	log ([S II]/Hα)	log ([O I]/Hα)	log M$_*$ (M$_\odot$)	(U-B)$_0$	Broad line[a]
1	>0.52	<-0.29	<0.08	<-0.18	$10.38^{0.21}_{0.05}$	0.98 ±0.03	
2	0.69 ±0.14	-0.07 ±0.05	<-0.40	<-0.62	$11.07^{0.06}_{0.07}$	0.99 ±0.02	
3	>0.01	-0.23 ±0.06	<-0.32	<-0.64	$10.96^{0.06}_{0}$	0.90 ±0.01	
4	0.22 ±0.06	-0.22 ±0.01	-0.62 ±0.04		$10.82^{0.03}_{0.07}$	0.57 ±0.01	Hα
5	>0.48				$11.13^{0.11}_{0.08}$	0.96 ±0.03	Hα
6b[b]	0.27 ±0.32	-0.22 ±0.04	-0.84 ±0.14	<-0.53	10.35[c] $^{0.49}_{0.16}$	0.70 ±0.11	
6r[d]	0.04 ±0.10	-0.46 ±0.09	-0.56 ±0.10	<-0.40	$10.35^{0.49}_{0.16}$	0.70 ±0.11	
7	<0.45	-0.19 ±0.05	-0.43 ±0.14	<-0.81	$10.92^{0.07}_{0.22}$	0.84 ±0.05	
8	1.22 ±0.13	-0.40 ±0.03	-0.86 ±0.09	-1.27 ±0.16	$10.66^{0.01}_{0.01}$	0.84 ±0.01	Hβ, [O III], Hα
9	>-0.46	-0.18 ±0.07	<-0.24	<-0.62	$11.23^{0.25}_{0.16}$	0.97 ±0.06	
10	0.72 ±0.07	-0.42 ±0.05	<-0.69	<-1.41	$10.66^{0.06}_{0.40}$	0.72 ±0.08	Hα

[a] where both a narrow and broad Gaussian fit was required
[b] bluer spectral component
[c] The stellar mass and color for this AGN are derived for the entire source, not the bluer and redder spectral components separately
[d] redder spectral component

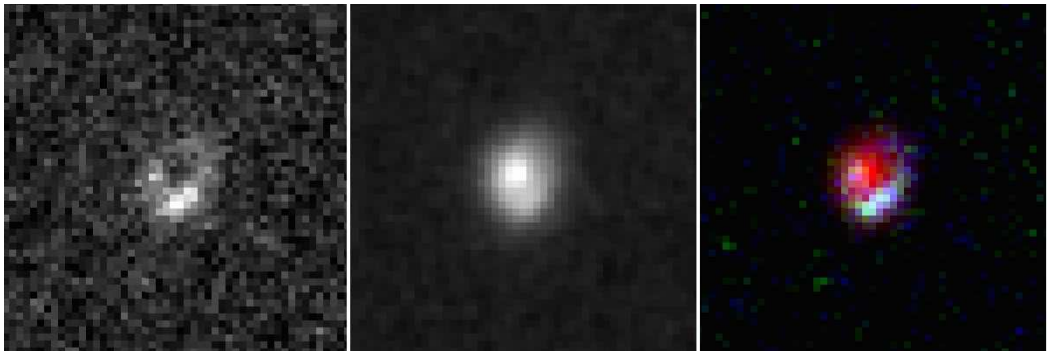

Fig. 2.— HST postage stamps for AGN ID 6. From left to right: the F606W image, the F160W image, and a color composite with R=F160W, G=F775W, B=F606W. Each postage stamp is 3″ on a side. This source has two kinematically distinct spectral components, separated by $\sim 120-200$ km s^{-1}. These HST images show that the two spectral components are likely associated with an on-going merger event.

rest frame for the narrow lines and 3.5 Å for the broader lines. Line ratios and 3σ limits for the AGN are given in Table 2.

Gaussian fits are also performed for MOSDEF galaxies that are not identified as AGN *a priori* using X-ray or IR imaging. To be consistent with the AGN fitting, we do not allow for a continuum slope for the galaxy line fits (though we note that allowing a slope does not change our results). We also include Balmer absorption corrections to both the Hα and Hβ line fluxes, for both galaxies and AGN, using results from SED fitting (see below). Typically, this correction to Hα and Hβ is only a few percent. Throughout the paper, in each figure we show MOSDEF galaxies that have $S/N \geq 3$ for each of the emission lines required for that figure.

As discussed above, AGN ID 6 displays two spectral components for each emission line. The two spectral components for this AGN are not substantially different in width; there is not a broad and narrow component but rather two narrow components, one at the rest wavelength and one bluer. The bluer component is offset by -115 km s^{-1} in [N II], -120 km s^{-1} in Hα, -205 km s^{-1} in [O III], and -203 km s^{-1} in Hβ, relative to the redder emission line at the rest wavelength. Fig. 2 shows HST postage stamps for this source. The F606W emission (left panel, Giavalisco et al. 2004) appears in a ring, with stronger emission on one side of the ring. This ring is filled in with F160W emission (middle panel, Grogin et al. 2011, Koekemoer et al. 2011), such that the color composite (right panel) shows a blue ring around a central red source. These images suggest that this object is undergoing a merger event, with tidal debris or triggered star formation seen in the F606W image. For this source we do not apply Balmer absorption corrections, as it is not clear how to apply a single correction derived from the SED, where both components are contributing to the light, to the individual redder and bluer spectral components. However, this correction should be negligible.

2.4. *Stellar Mass and Rest-frame Color Measurements*

Stellar masses for MOSDEF galaxies and AGN are estimated from SED fits to the 3D-HST multi-wavelength photometry (Skelton et al. 2014) using the FAST SED fitting code of Kriek et al. (2009), with the Conroy et al. (2009) stellar population synthesis models and the Chabrier (2003) initial mass function (IMF). Errors are derived by perturbing the photometry according to the photometric errors and remeasuring the stellar mass. The 16th and 84th percentiles of the resulting distribution are taken to be the lower and upper error bounds on the stellar, respectively. Rest-frame $(U-B)_0$ colors are estimated from the best-fit template in the FAST SED fitting process, using Bessel U and B filter curves. Error bars on the rest-frame $(U-B)_0$ colors are derived from the input photometry and associated error bars,

where we perturb each photometric point by a Gaussian random variable with the width set by the photometric error for that point. The standard deviation which results from doing this 500 times is used to derive the error on the $(U-B)_0$ color.

For the AGN, we do not include u-band or IRAC photometry when deriving stellar masses and rest-frame colors, to avoid contamination due to the AGN light. We do use these bands in the SED fits to the galaxies. We find that none of our results change if we include the u-band and IRAC photometric points for the AGN, though the exact stellar masses and rest-frame colors for some AGN change slightly (the median difference in stellar mass is 0.05 dex). Stellar masses and $(U-B)_0$ colors for the AGN are given in Table 2.

For comparison purposes, we also compile line ratios, stellar masses, and rest-frame $(U-B)_0$ colors for galaxies and AGN in the SDSS. We restrict the SDSS sample to sources with $z < 0.2$ and show only those sources with S/N>3 in all of the relevant emission lines used for a particular diagnostic. Line ratios and stellar masses are taken from the SDSS Data Release 7 (DR7) emission line and stellar mass catalogs developed by the Max-Planck Institute for Astronomy (Garching) and John Hopkins University (MPA/ JHU). The methodology for measurements of emission-line fluxes is described by Tremonti et al. (2004). Balmer absorption corrections have been applied to these SDSS line fluxes. Stellar masses are based on SED fits, following the methodology of Kauffmann et al. (2003) and Salim et al. (2007), and use the Bruzual & Charlot (2003) stellar population synthesis models and the Chabrier (2003) IMF. Rest-frame $(U-B)_0$ colors are taken from the best-fit SED template using `iSEDfit` outputs from Moustakas et al. (2013). The SED fits use photometry spanning the ultraviolet ($GALEX$) through the optical to the mid-infrared ($WISE$) and use the Conroy et al. (2009) models and the Chabrier (2003) IMF. The differences in how the stellar masses and rest-frame colors are derived in SDSS compared to MOSDEF are small and do not affect any of our conclusions.

3. RESULTS

In this section we present the location of MOSDEF galaxies and AGN, identified either through X-ray or IR emission, in the various optical AGN diagnostic figures, including the BPT, MEx, and CEx diagrams. We compare their locations with local SDSS galaxies as well as the various proposed classifications between star-forming galaxies and AGN in these diagrams.

3.1. *BPT Diagram*

In Fig. 3 we show the [O III]/Hβ versus [N II]/Hα BPT diagram (Baldwin et al. 1981; Veilleux & Osterbrock 1987) for our MOSDEF AGN (red and purple circles) and galaxies (blue triangles). MOSDEF targets that are identified as AGN from their IRAC colors are marked with a purple circle, while X-ray AGN are shown with red circles. For the AGN with two spectral components (ID 6) we plot each component separately; '6b' indicates the bluer component, while '6r' indicates the redder component. It is possible that only one of these components contains an AGN. For clarity, only those MOSDEF galaxies with at least 3σ detections in all four lines used for this diagram are shown here; this results in a sample of 50 MOSDEF galaxies. We note that the Balmer absorption corrections are typically small ($\sim$ 0.01 dex in [N II]/Hα and $\sim$ 0.06 dex in [O III]/Hβ) for galaxies and AGN and do not affect their location in the BPT diagram substantially.

For comparison we show the distribution of SDSS sources with contours and greyscale; we show all SDSS sources in DR7 that have S/N> 3 for Hβ, [O III], [N II], and Hα. The dashed dark green line indicates the local empirical division between star-forming galaxies and AGN from Kauffmann et al. (2003), while the dot-dash dark green line indicates the local theoretical "maximum" allowed starburst galaxy in Kewley et al. (2001). At $z \sim 0$ sources above the latter division have line ratios that can only be due to AGN, in the models of Kewley et al. (2001). Sources in between these two divisions are often referred to as "composite" sources, where there are contributions to the line ratios from both star formation and AGN activity. A more complete local optical AGN sample would therefore include these "composite" sources.

As discussed in the introduction, many authors have found that galaxies at $z \sim 1-3$ are offset in the BPT diagram when compared with local samples. Similarly, here we find that the MOSDEF galaxies have, on average, slightly higher [O III]/Hβ ratios at a given [N II]/Hα ratio (or equivalently, higher [N II]/Hα at a given [O III]/Hβ), compared to SDSS galaxies. We find that the vast majority of MOSDEF galaxies not identified as X-ray or IR AGN lie below the Kauffmann et al. (2003) division, and only two MOSDEF galaxies lie above the Kewley et al. (2001) line. The latter are identified in Fig. 3 with cyan outlines. We also outline in light green the four additional galaxies above the Kauffmann et al. (2003) line. Here we consider these galaxies as potential optical AGN candidates, given their location in the BPT diagram with respect to local AGN classification lines.

We note that of the nine MOSDEF X-ray and IR AGN (one with two spectral components) shown here, four have limits in [O III]/Hβ (three lower limits and one upper limit), one of which also has an upper limit in [N II]/Hα, as indicated with red arrows. Five of the MOSDEF AGN lie above the Kewley et al. (2001) line (though one is an upper limit in [N II]/H$\alpha$and another an upper limit in [O III]/Hβ), while AGN ID '6b' is just below the line, with an [O III]/Hβ error that extends well above the line. AGN ID 4 is also just below the line, 1.3σ away. There are two additional AGN (ID 3 and 9) in the "composite" region that have lower limits in [O III]/Hβ such that they could potentially be above the Kewley et al. (2001) line. Only AGN ID '6r' clearly falls well below the Kewley et al. (2001) line; it is just below the Kauffmann et al. (2003) line. As discussed above, AGN ID 6 is an X-ray source and contains an AGN, but we do not know whether the AGN is associated with the redder or bluer spectral component (or both). Therefore it could be that the bluer component has an AGN, and indeed the BPT diagram strongly suggests that this is likely. We therefore find that our X-ray and IR AGN are either above or consistent with being above the Kewley et al. (2001) line.

This figure clearly shows that both the [O III]/Hβ and [N II]/Hα ratios are necessary to separate AGN from

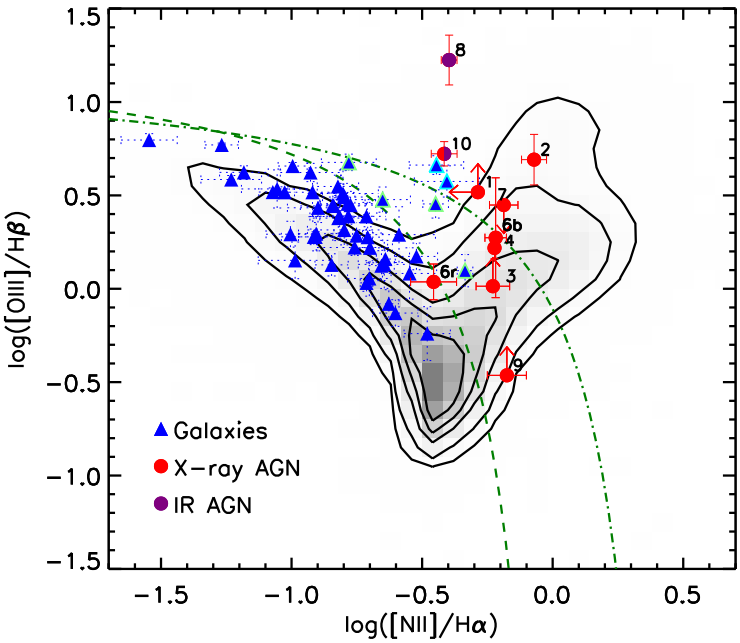

FIG. 3.— The [O III]/Hβ versus [N II]/Hα BPT diagram for MOSDEF galaxies and AGN at $z \sim 2.3$. Contours and greyscale show the locations of SDSS sources, while blue triangles show MOSDEF galaxies and circles MOSDEF AGN, identified as AGN either through X-ray (red circles) or IR emission (purple circles). One AGN (ID 10) is both an X-ray and IR-identified AGN. In this and subsequent figures, SDSS contours are shown for 30%, 50%, 70%, 90%, and 97% of the sources. Arrows indicate 3σ limits for AGN that are not detected in all four lines. The dashed and dot-dash green lines show the $z \sim 0$ divisions between star-forming galaxies (below the lines) and AGN (above the lines) from Kauffmann et al. (2003) and Kewley et al. (2001), respectively. We outline two MOSDEF galaxies that are above the Kewley et al. (2001) line in cyan and four additional galaxies above the Kauffmann et al. (2003) line in light green.

galaxies at $z \sim 2.3$, and that of the two line ratios, the [N II]/Hα ratio has much more discriminatory power in that all of the MOSDEF AGN have [N II]/Hα of $\gtrsim$-0.5, while they span a wide range of [O III]/Hβ values. It appears that at the depth of the MOSDEF survey the [N II]/Hα ratio alone may be sufficient to separate AGN from galaxies at these redshifts (see also Stasińska et al. (2006)).

As to whether divisions between star-forming galaxies and AGN such as the Kauffmann et al. (2003) and Kewley et al. (2001) lines can be applied at $z \sim 2$, Fig. 3 shows that because galaxies at these redshifts are offset, on average, with respect to SDSS sources these divisions need to be revised slightly ($\sim$0.1-0.2 dex) such that galaxies are not included in AGN samples. We return to this point in section 4.1 below.

3.2. *[S II]/Hα and [O I]/Hα BPT Diagrams*

In Fig. 4 we show the other two BPT-like diagrams that are commonly used at low redshift to separate star-forming galaxies and AGN (Veilleux & Osterbrock 1987). On the left is the [O III]/Hβ versus [S II]/Hα diagram, and on the right is the [O III]/Hβ versus [O I]/Hα diagram. The left panel includes 56 MOSDEF galaxies, where we include all galaxies with S/N $>$ 3 in each of the four lines used for this figure. Open blue triangles show galaxies that have S/N $>$ 3 in the sum of the [S II] lines but S/N $<$ 3 in the [N II] λ6585 line, such that they are not shown in Fig. 3. 10 of these twelve galaxies have S/N $>$ 2 in the [N II] λ6585 line, with values of log [N II]/Hα $<$ $-$0.8 such that they would not be classified as AGN in the BPT diagram. The two MOSDEF galaxies in the BPT diagram in Fig. 3 that are above the Kewley et al. (2001) line are shown here with cyan outline, and the four additional galaxies above the Kauffmann et al. (2003) line are shown with light green outlines, as in Fig. 3. We note that MOSDEF galaxies do not have, on average, higher [O III]/Hβ at a given [S II]/Hα ratio, unlike at a given [N II]/Hα ratio, as seen above (see also Shapley et al. 2014.

In the [S II]/Hα diagram the MOSDEF AGN lie throughout the entire range of the MOSDEF galaxies in both [S II]/Hα and [O III]/Hβ. Five of the AGN have upper limits in [S II]/Hα. Five of the MOSDEF AGN (along with many MOSDEF galaxies) lie above the local "maximal" starburst line from Kewley et al. (2001), and the other four AGN (one with two spectral components) lie below it. Those AGN that are below the Kewley et al. (2001) line in this diagram are also those that are in the "composite" region in Fig. 3. This is consistent with studies that have shown that at low redshift, "composite" sources often lie below the Kewley et al. (2001) line in the [S II]/Hα diagram (e.g., Stern & Laor 2013). There is one MOSDEF AGN (ID 1) in the LINER region of this diagram, though given that it has limits in both line ratios such that it could fall in the Seyfert region. We therefore do not classify any of our X-ray/IR AGN as LINERs. Given the high overlap between the MOSDEF galaxies and AGN in this figure, it appears that that [S II]/Hα versus [O III]/Hβ diagram does not have as much discriminatory power at $z \sim 2$ to identify AGN. We note that of the four "composite" sources outlined in light green, three lie near or above the Kewley et al. (2001) line, such that they would be classified as AGN, though there are an additional nine MOSDEF galaxies also above this line that are below the Kauffmann et al.

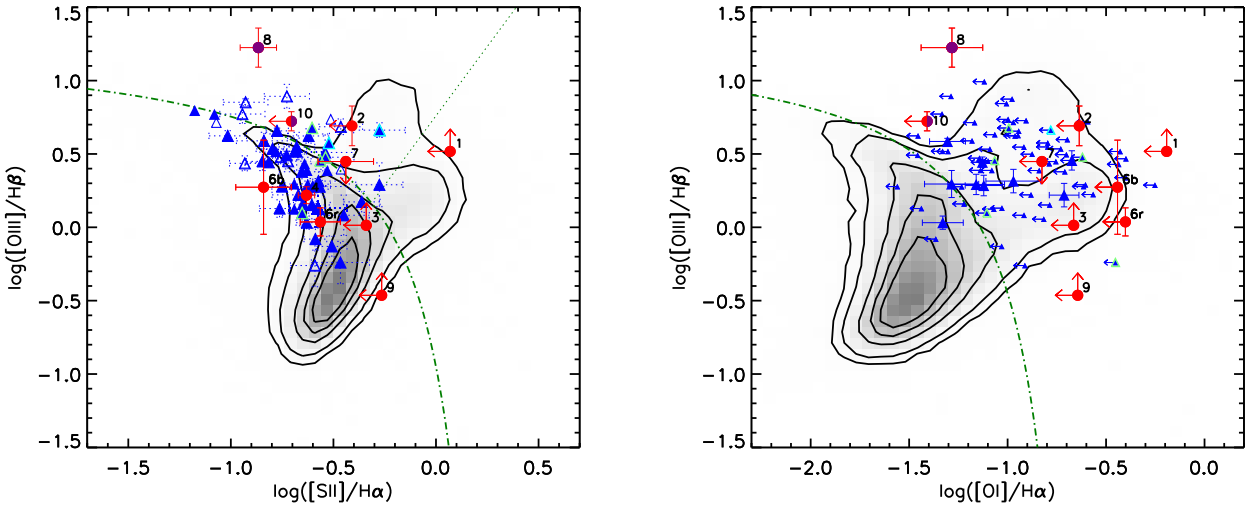

FIG. 4.— The [O III]/Hβ versus [S II]/Hα (left) and [O III]/Hβ versus [O I]/Hα (right) diagrams for MOSDEF galaxies and AGN at $z \sim 2.3$. As in Fig. 3, contours and greyscale show the locations of SDSS sources, while blue triangles show MOSDEF galaxies and red and purple circles MOSDEF AGN, identified as AGN either through X-ray or IR emission. Arrows indicate 3σ limits for AGN and galaxies (right panel) that are not detected in all four lines. Open blue triangles show galaxies that are not included in Fig. 3, due to low S/N in [N II] and/or Hα. The dot-dash green lines show the $z \sim 0$ divisions between star-forming galaxies (below the line) and AGN (above the line) from Kewley et al. (2001), while the dotted green line in the left panel shows the division between Seyfert AGN and LINERs from Kewley et al. (2006). The two MOSDEF galaxies in Fig. 3 that are above the Kewley et al. (2001) line in the BPT diagram are outlined here in cyan, and four additional galaxies above the Kauffmann et al. (2003) line are outlined in light green. In the right panel, most MOSDEF sources have upper limits in [O I]/Hα, though one AGN and eight galaxies have $> 3\sigma$ detections.

(2003) line in the BPT diagram. It therefore appears that the Kewley et al. (2001) classification in the [O III]/Hβ versus [S II]/Hα diagram is not as useful in reliably identifying AGN at $z \sim 2$ compared to the classification in the BPT diagram.

The right panel of Fig. 4 shows the [O III]/Hβ versus [O I]/Hα diagram, where here we show all MOSDEF galaxies with $> 3\sigma$ detections in [O III]/Hβ, regardless of whether they have a detection in [O I]. This results in a sample of 71 galaxies. For most MOSDEF galaxies and AGN we have only upper limits in [O I]. There are eight galaxies and one AGN for which we have $> 3\sigma$ detections in [O I] and Hα, shown here with error bars (all of these sources are shown in Fig. 3). The one detected AGN is above the Kewley et al. (2001) division, as are all but one of the MOSDEF galaxies that are detected. It is difficult to draw conclusions from this figure, given how many sources are not detected, but having seven sources that were not identified as AGN from either X-ray or IR emission above the Kewley et al. (2001) line might indicate that at $z \sim 2$ galaxies and AGN do not separate as cleanly in this space as they do at $z \sim 0$.

3.3. *MEx Diagram*

In Fig. 5 we show the MEx diagram of Juneau et al. (2011), where here we show all MOSDEF galaxies that have $> 3\sigma$ detections in both [O III] and Hβ; this results in a sample of 87 galaxies. The 37 additional galaxies shown here that are not shown in Fig. 3 due to having S/N<3 in the [N II] and/or Hα lines are plotted with open blue triangles. The vast majority of them are likely not AGN, given that $\gtrsim 90\%$ of the galaxies in Fig. 3 are not identified as AGN, and these additional galaxies do not have strong [N II] lines. For AGN ID 6, here we plot only the bluer spectral component, as this component in the BPT diagram is in the AGN region, while the redder spectral component is below the Kauffmann et al. (2003) line. For this source we only have a stellar mass for the entire object, not a mass associated with each spectral component; the stellar mass is therefore overestimated.

In the MEx diagram the dot-dashed green lines show the divisions suggested in this space between star-forming galaxies, composite galaxies, and AGN in SDSS from Juneau et al. (2014). It is immediately clear that these divisions are not appropriate for our sources at $z \sim 2.3$. Juneau et al. (2014) predict a shift in these divisions to higher stellar mass for high redshift surveys. They use a functional form describing the evolution of $L^*_{H\alpha}$ (the break in the Hα luminosity function), to essentially track the evolution in the global SFR density. This is then combined with the Hα and [O III] line luminosity detection limits in a given high redshift survey, to select galaxies in SDSS that have similar line luminosities relative to $L^*_{H\alpha}$ (at $z \sim 0$) as galaxies in the high redshift survey (relative to $L^*_{H\alpha}$ at the redshift of the survey). They then use the separation of star-forming galaxies and AGN from this "similarly-selected" sample in SDSS to determine how much the MEx dividing lines should shift to higher mass, for a given high redshift survey. Essentially, they predict that for high redshift spectroscopic surveys, especially those that are not particularly deep, the MEx divisions between star-forming galaxies and AGN should shift to higher stellar mass because galaxies and AGN with higher line luminosities populate the "upper" region of the MEx diagram, such that the division between star forming galaxies and AGN shifts to higher masses (see their Fig. 3).

The MOSDEF survey is fairly sensitive; in our $z \sim 2.3$ sample we detect at 3σ Hα fluxes down to $\sim 8 \times 10^{-18}$ erg s^{-1} cm^{-2}. The resulting line luminosity detection limit for both Hα and [O III] is $\sim 10^{41.5}$ erg s^{-1}. Given the redshift of the sample and the prescriptions in Juneau et al. (2014), the MEx divisions should there-

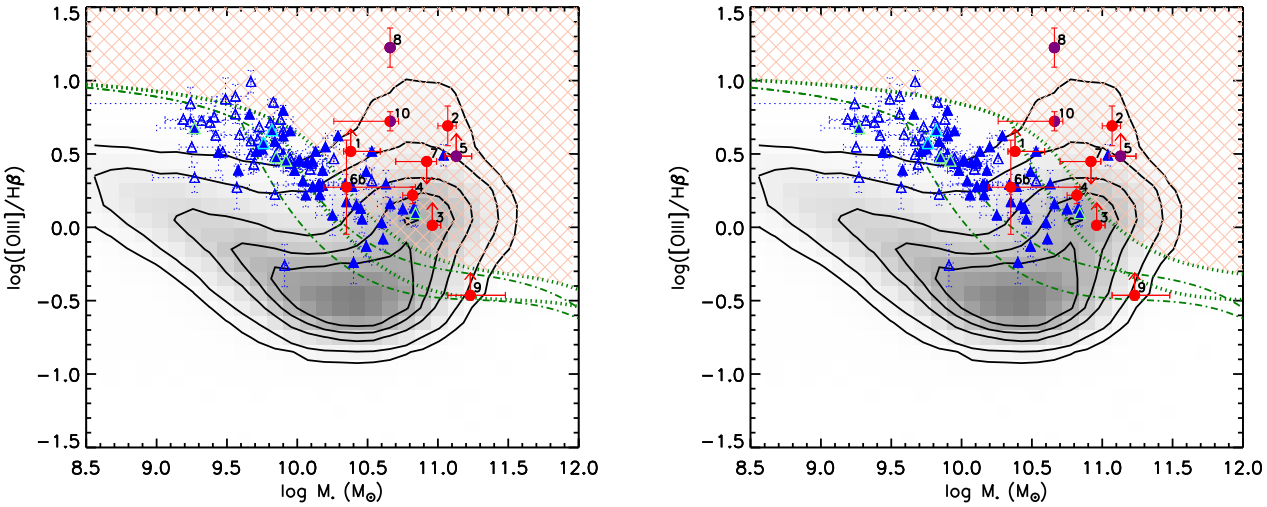

FIG. 5.— The mass excitation (MEx) diagram for MOSDEF galaxies and AGN at $z \sim 2.3$. As in previous figures, contours and greyscale show the locations of SDSS sources, while blue triangles show MOSDEF galaxies and red and purple circles MOSDEF AGN, identified as AGN either through X-ray or IR emission. Arrows indicate 3σ limits for AGN that are not detected in either [O III] and Hβ. Open blue triangles show galaxies that are not included in Fig. 3, due to low S/N in [N II] and/or Hα. The two MOSDEF galaxies in Fig. 3 that are above the Kewley et al. (2001) line in the BPT diagram are outlined here in cyan, and four additional galaxies above the Kauffmann et al. (2003) line are outlined in light green. The dot-dash dark green lines indicate the divisions between star-forming galaxies and AGN in SDSS from Juneau et al. (2014). The dotted dark green lines in the left panel indicate shifts in the Juneau et al. (2014) classifications to higher stellar mass, based on the Hα and [O III] luminosity limits of our $z \sim 2.3$ sample. The red shaded region indicates the space above this line which should be populated almost exclusively by AGN. The predicted shift of $\Delta\log(M_*/M_\odot) = 0.25$ (left panel) leads to serious contamination of the AGN region with star-forming galaxies. We find that a stellar mass shift of $\Delta\log(M_*/M_\odot) = 0.75$ (dotted green lines, right panel) is required to more effectively separate star-forming galaxies and AGN at $z \sim 2.3$ for MOSDEF sources.

fore shift to higher stellar mass by $\Delta\log(M_*/M_\odot) = 0.25$ for our sample. However, as seen by the dotted green lines in the left panel of Fig. 5, shifting the divisions by this amount is clearly insufficient to cleanly separate star-forming galaxies and AGN in our sample; there are many galaxies in the red shaded region, which highlights the upper part of the AGN region (above the higher of the two green dotted lines). Instead we find that a substantially higher shift of $\Delta\log(M_*/M_\odot) = 0.75$ is needed (Fig. 5, right panel), so as not to contaminate the AGN region of this diagnostic figure with star-forming galaxies. We note that Newman et al. (2014) also found that a similarly large shift in the MEx diagram is needed to separate star-forming galaxies and AGN in their $z \sim 2$ galaxy sample (see also Henry et al. 2013; Price et al. 2014). Such a large shift is needed to match the stellar masses of local and $z \sim 2$ galaxies with the same metallicity (Steidel et al. 2014; Sanders et al. 2014), as galaxies at a given stellar mass have higher [O III]/Hβ at higher redshift, due to having lower metallicity. Therefore, the shift required appears to depend more upon the evolution in the mass-metallicity relation of galaxies and therefore the redshift, rather than the depth, of a given survey.

With our proposed shift of $\Delta\log(M_*/M_\odot) = 0.75$ we find that five of our ten X-ray and IR-selected AGN are in the AGN-only region of this diagram, two are in the AGN/star-forming region (between the two dotted lines), and another two (ID 1 and 6b) could be within this region given their stellar mass errors (and the lower limit on [O III]/Hβ for ID 1). ID 9 has a lower limit in [O III]/Hβ, such that it could be in this region as well. Therefore all of our X-ray/IR AGN are consistent with being identified as AGN in this diagram.

Using the more extreme classification in the right panel of Fig. 5, there is one MOSDEF galaxy clearly in the red shaded region (above the upper dotted green line) of the diagram, with log $M_* = 11.04$. This source has log ([O III]/Hβ) = 0.491 and log ([N II]/Hα) = -0.80; in the BPT diagram it is in the star-forming sequence, 1.3σ from the Kauffmann et al. (2003) line. The X-ray upper limits for this source are log (L_X/(erg s^{-1})) = 42.9 in the hard band and log (L_X/(erg s^{-1})) = 42.2 in the soft band. While the X-ray data are not deep enough to rule out an AGN, the [N II]/Hα ratio is more consistent with star formation, not AGN activity. This appears to be a particularly massive galaxy that is not an AGN, even though the MEx classification would identify it as such. There is another MOSDEF galaxy in the AGN region, with log $M_* = 9.65$.; within the errors on [O III]/Hβ it could be below the AGN classification line, however the high [O III]/Hβ ratio could also indicate the presence of an AGN.

We further note that one of the "composite" MOSDEF galaxies with a high [N II]/Hα, which is outlined in light green, is in the AGN/star-forming galaxy region of this diagram, and it may well be an AGN. The other four "composite" galaxies above the Kauffmann et al. (2003) line, however, are well below the AGN classification lines and are in the middle of the MOSDEF galaxy sample, as are the two galaxies outlined in cyan which are above the Kewley et al. (2001) line.

There are several additional MOSDEF galaxies in the "composite" AGN region of this figure (between the two dotted lines), using our proposed stellar mass shift. All of these galaxies fall below the Kauffmann et al. (2003) line in the BPT diagram. They are therefore likely star-forming galaxies without any AGN contribution to their line ratios and are contaminants in the MEx diagram. However, given that the region between the two classi-

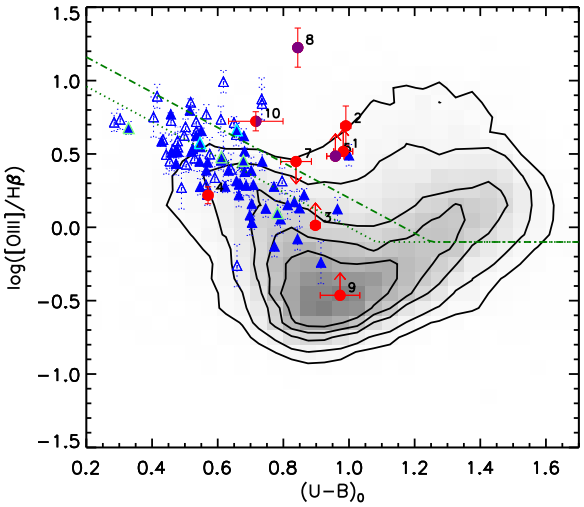

FIG. 6.— The color excitation (CEx) diagram for MOSDEF galaxies and AGN at $z \sim 2.3$. The colors and contours are the same as in Fig. 5. The dot-dashed dark green lines indicate the division between star-forming galaxies and AGN in SDSS from Yan et al. (2011), while the dotted green line shows the same division shifted blueward by 0.2 mag (Trump et al. 2013).

fication lines in the MEx diagram is defined to contain ∼50% star-forming galaxies and 50% AGN, some contamination from star-forming galaxies is allowed. Overall, the MEx diagram appears to be fairly complete for our X-ray and IR-selected AGN, using the larger shift in stellar mass found here.

3.4. *CEx Diagram*

In Fig. 6 we show the CEx diagram of Yan et al. (2011), which is similar to the MEx diagram but uses rest-frame $(U-B)_0$ color instead of stellar mass as a proxy for [N II]/Hα in order to effectively separate AGN from star-forming galaxies. We do not plot AGN ID 6 in this diagram, as we do not have colors estimated for each of the two spectral components separately, only a composite color for the entire galaxy.

The dividing line proposed for this diagnostic by Yan et al. (2011) (dot-dashed dark green line) is calibrated using SDSS data and the location of BPT-identified AGN, but Yan et al. (2011) show that to $z = 0.4$ it works well, when compared to X-ray selected AGN. They claim that the CEx diagram and their proposed division between AGN and star-forming galaxies can be used to $z \sim 1$, and that while galaxies at $z \sim 1$ are bluer in $(U-B)_0$ than galaxies at $z \sim 0$ by ∼0.14 mag, this difference is small and therefore not applied in their application of the CEx diagram to $z \sim 1$. Trump et al. (2013) propose that for galaxies at $z \sim 1.5$ the CEx classification line should shift by 0.2 mags to bluer colors, where X-ray AGN were used to determine the shift at $z \sim 1.5$. The dotted green line in Fig. 6 shows this shifted line.

While the locus of MOSDEF galaxies on this figure, relative to the location of the bulk of SDSS galaxies, shows that indeed galaxies are bluer on average at $z \sim 2$ than locally, there is no clean division between MOSDEF X-ray/IR AGN and galaxies in this space. While many of the reddest MOSDEF sources at $z \sim 2.3$ are AGN, there are also AGN with bluer colors. There are also many galaxies above the proposed AGN classification line. Using the revised Trump et al. (2013) division results in even more contamination by star-forming galaxies than the original Yan et al. (2011) division (see Section 4.4 below.)

Cimatti et al. (2013) also find that at $1.7 < z < 3$ there are many X-ray AGN in the blue cloud (21% of X-ray AGN are in the blue cloud in their sample), and that at $1 < z < 1.7$ the fraction of AGN on the red sequence rises. The reason the CEx diagram works at lower redshift is that at late cosmic times the most massive galaxies are generally red and quiescent. The red color of a galaxy can be used as a proxy for high stellar mass. However, at $z \sim 2$ massive galaxies show a large diversity in galaxy properties and colors (Kriek et al. 2008; Brammer et al. 2011; Barro et al. 2013; Ilbert et al. 2013; Muzzin et al. 2013). As seen in Fig. 8 in Muzzin et al. (2013), for galaxies with log $(M_*/M_\odot) > 11$, below $z \sim 1.7$ there are more quiescent galaxies, while above $z \sim 1.7$ there are more star-forming galaxies. From the results presented here we conclude that the CEx diagram can not be reliably used at $z \sim 2.3$ for AGN/star-forming galaxy classification.

4. DISCUSSION

In this paper we test the widely-used optical locally-calibrated AGN diagnostics at $z > 2$ using a statistical sample of ∼50 galaxies and 10 X-ray and/or IR-selected AGN from the MOSDEF survey. We find that the BPT diagram remains a useful diagnostic for separating star-forming galaxies and X-ray and IR-selected AGN at $z \sim 2$. Below we discuss what classification line(s) should be used at this redshift to identify AGN; we compare the Kauffmann et al. (2003) and Kewley et al. (2001) classification lines at $z \sim 0$ with the updated Kewley et al. (2013b) line at high redshift and discuss the use of these classifications at $z \sim 2$. We also discuss the completeness of AGN samples selected using the BPT diagram at low and high redshift, as well as the completeness of the MEx diagnostic. We also discuss the metallicities of $z \sim 2$ AGN and whether "contamination" by weak AGN may be causing a shift in the $z \sim 2$ galaxy population in the BPT diagram.

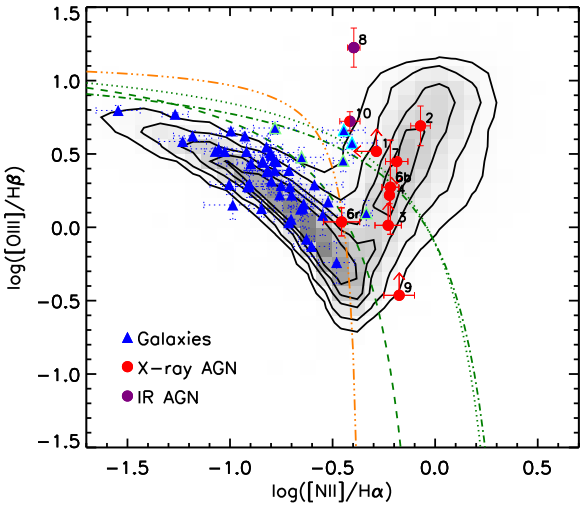

FIG. 7.— Same as Fig. 3 but here the contours and greyscale are shown only for SDSS sources with [O III] and Hα line luminosities greater than the MOSDEF limit. The additional dark green dotted line shows the predicted upper limit for star-forming galaxies at $z \sim 2.3$ from Kewley et al. (2013b), and the dot-dot-dash orange line shows the predicted theoretical line from Meléndez et al. (2014) above which sources have an AGN contribution.

TABLE 3
OPTICAL AGN CANDIDATE SOURCE INFORMATION

Field	ID [a]	RA	Dec	z	log L_X [b] (erg s^{-1})	log ([O III]/Hβ)	log ([N II]/Hα)	log ([S II]/Hα)	log M$_*$ (M$_\odot$)	(U-B)$_0$
COSMOS	1740[d e]	10:00:14.161	02:11:51.627	2.29986	< 43.44	0.45 $\pm$0.08	-0.45 $\pm$0.05	-0.56 $\pm$0.10	$9.92^{+0.06}_{-0.00}$	0.68
COSMOS	2786[c]	10:00:14.301	02:12:26.264	2.29807	<43.68	0.57 $\pm$0.08	-0.41 $\pm$0.12	-0.52 $\pm$0.14	$9.76^{+0.08}_{-0.12}$	0.55
COSMOS	2575	10:00:14.795	02:12:19.395	2.31585	<43.44		-0.29 $\pm$0.10	<-0.31	$10.94^{+0.00}_{-0.06}$	1.11
COSMOS	3182	10:00:18.241	02:12:42.586	2.10206	<43.40		-0.22 $\pm$0.03	-0.63 $\pm$0.08	$11.40^{+0.07}_{-0.00}$	1.36
COSMOS	11597[c]	10:00:21.720	02:17:50.358	2.52736	< 43.62	0.66 $\pm$0.05	-0.45 $\pm$0.10	-0.28 $\pm$0.13	$9.82^{+0.09}_{-0.22}$	0.66
GOODS-N	26458	12:36:57.389	62:16:18.140	2.48636	<43.04		-0.34 $\pm$0.09		$10.32^{+0.02}_{-0.08}$	0.68
GOODS-N	22457[d]	12:37:10.679	62:15:07.182	2.46938	< 42.70	0.48 $\pm$0.07	-0.65 $\pm$0.11	-0.54 $\pm$0.14	$9.85^{+0.04}_{-0.06}$	0.61
GOODS-N	28846[d]	12:37:13.096	62:17:03.225	2.47198	< 43.13	0.68 $\pm$0.04	-0.78 $\pm$0.10	-0.60 $\pm$0.13	$9.27^{+0.12}_{-0.27}$	0.33
GOODS-N	13088[d e]	12:37:20.054	62:12:22.854	2.46015	< 43.19	0.10 $\pm$0.09	-0.34 $\pm$0.03	-0.65 $\pm$0.10	$10.84^{+0.01}_{-0.10}$	0.78

[a] ID in 3D-HST v4.1 catalogs
[b] in the 2-10 keV hard band
[c] above the Kewley et al. (2013a) AGN classification line
[d] above the Kauffmann et al. (2003) AGN classification line
[e] above the Meléndez et al. (2014) AGN classification line

4.1. *Classifying Star-Forming Galaxies and AGN in the BPT Diagram at $z \sim 2$*

We find that using the $z \sim 0$ demarcations to classify optical AGN in our MOSDEF sample leads to only two additional sources being classified as "pure" AGN, i.e., above the Kewley et al. (2001) line, and four sources classified as "composite", in between the Kauffmann et al. (2003) and Kewley et al. (2001) lines. As the hard band X-ray upper limits on most MOSDEF galaxies is only log (L_X/(erg s^{-1})) $\sim$ 43, and given that IR AGN selection tends to identify only luminous AGN (Mendez et al. 2013), it is plausible that at least some, if not all, of these sources are AGN.

As we have shown, however, at $z \sim 2$ galaxies lie somewhat above the main locus of star-forming galaxies in SDSS (see also e.g., Yabe et al. 2012; Masters et al. 2014; Steidel et al. 2014; Newman et al. 2014; Shapley et al. 2014). Due to this "offset" of galaxies in the BPT at high redshift, it is likely that the demarcations used to separate star-forming galaxies from AGN in SDSS at $z \sim 0$ need to be shifted somewhat at high redshift.

However, there is somewhat less of an "offset" in the BPT diagram if high redshift galaxies are compared with SDSS galaxies with a similar line luminosity limit (Juneau et al. 2014). In Fig. 7 we show the BPT diagram with MOSDEF galaxies and AGN as above in Fig. 3, but here we show only SDSS sources with Hα and [O III] luminosities greater than the MOSDEF limit of $\sim 10^{41.5}$ergs^{-1}. There is less of an offset for MOSDEF galaxies in this figure, compared to Fig. 3, though at a given [N II]/Hα the MOSDEF galaxies have a slightly higher log ([O III]/Hβ) by $\sim$0.1 dex. Shapley et al. (2014) fit the MOSDEF galaxy locus in the BPT diagram, and when compared to the fit by Kewley et al. (2013a) for all SDSS sources, at [N II]/Hα = -1.0 the [O III]/Hβ values in the MOSDEF fit are high by 0.12 dex. The sample of Steidel et al. (2014) is more offset, but as discussed in Shapley et al. (2014) et al. this is due

to differences in the sample selection.

Kewley et al. (2013b) propose a new redshift-dependent semi-empirical demarcation between pure star-forming galaxies and those with contributions from an AGN, using their theoretical models. Sources above this line should be "composite" sources. In Fig. 7 we show the proposed Kewley et al. (2013b) line indicated with a dark green dotted line for the median redshift of our sample, $z = 2.3$. The $z \sim 0$ classification of Kewley et al. (2001) is shown with a dot-dashed dark green line. At $z = 2.3$ there is not a substantial difference between these classifications, though the redshift-dependent line does allow galaxies at high redshift to have somewhat higher [O III]/Hβ ratios (log ([O III]/Hβ) for galaxies is <0.1 dex higher at low [N II]/Hα in the updated demarcation). The lines have different physical motivations, however, in that "composite" sources at $z \sim 0$ should be below the Kewley et al. (2001) line and at $z \sim 2.3$ should be above the Kewley et al. (2013b) line.

We find that five of the nine MOSDEF X-ray and IR-selected AGN are above the Kewley et al. (2013b) line, and of the four AGN below these lines, two are lower limits in [O III]/Hβ such that they could be higher and another is above the line within the error bars. AGN ID '6r' is a spectral component that may not correspond to an AGN. Using either the Kewley et al. (2001) or Kewley et al. (2013b) lines to identify AGN, the two MOSDEF galaxies outlined in cyan would be classified as optical AGN. While the Kewley et al. (2013b) classification appears to reliably identify AGN at $z \sim 2$, it is not clear that it includes "composite" sources at $z \sim 2$, as using either the Kewley et al. (2001) or Kewley et al. (2013b) lines limits AGN samples by preferentially excluding AGN with star-forming host galaxies (see next section below).

At low redshift, using the Kauffmann et al. (2003) classification line results in a more complete AGN sample and allows one to determine whether the line ratios from a source are purely from star formation or have some contribution from AGN activity. If indeed ISM conditions at high redshift differ from those in nearby galaxies (discussed in Section 4.4 below), then the Kauffmann et al. (2003) line would need to evolve with redshift, but not as substantially as the proposed Kewley et al. (2013b) line. From Fig. 7 it appears that the "composite" classification needs to shift by ∼0.1-0.2 dex at $z \sim 2$ so as not to be contaminated by star-forming galaxies. Using the proposed AGN classification line of Stasińska et al. (2006), which is below the Kauffmann et al. (2003) line, one would classify 18 MOSDEF galaxies as AGN; clearly at $z \sim 2$ this classification suffers from contamination by star-forming galaxies and should not be used.

Recently, Meléndez et al. (2014) use photoionization models that include from both starburst galaxies and AGN to predict a curve in the BPT diagram showing where sources have a minimal contribution from an AGN. This line can therefore be used to separate star-forming galaxies from AGN, and it provides a new theoretical alternative classification scheme to the empirical Kauffmann et al. (2003) line. In Fig. 7 we show the Meléndez et al. (2014) prediction as a dot-dot-dash orange line. We show the predicted line that does not include dust; including dust shifts the line ∼0.1 dex higher. All of the MOSDEF X-ray/IR AGN are above this line, and using this classification scheme there are four additional optical AGN. Two of these sources are also above the Kewley et al. (2013b) line and two are composite sources above the Kauffmann et al. (2003) line. The two composite sources have relatively high [N II]/Hα and are closer in the BPT diagram to the X-ray/IR AGN and further from the bulk of the MOSDEF galaxies than the other two composite sources that are not identified as AGN using this new line. With the initial MOSDEF dataset we therefore find that this new classification scheme appears to work well at $z \sim 2$.

For now we consider all six sources above the Kauffmann et al. (2003) line as potential optical AGN candidates. Information on these sources is given in Table 3. (The additional three sources listed in Table 3 are discussed below in Section 4.5.) The hard band X-ray upper limits are all $\sim 10^{43}$ erg s^{-1} and do not rule out the presence of an AGN. Of the two optical AGN candidates above the Kewley et al. (2013a) line (IDs 11597 and 2786), one source (ID 11597) also has a high [S II]/Hα ratio and is separated from the star-forming galaxies in the left panel of Fig. 4. It is therefore likely to be an AGN. We note that while both candidates above the Kewley et al. (2013a) line have high [O III]/Hβ and [N II]/Hα ratios, neither is in the AGN region of the MEx diagram as both have stellar masses log (M_*/M$_\odot$) < 10. Of the four composite sources, ID 13088 has high [N II]/Hα (> -0.35) and also satisfies the Donley et al. (2012) IR AGN color selection criteria (while it does not strictly satisfy the criteria of $f_{8.0\mu m} > f_{5.8\mu m}$, it does within the 1.1 σ error). A second source (ID 1740) has a similar [N II]/Hα as the two sources above the Kewley et al. (2013a) line and is above the Meléndez et al. (2014) line. The other two sources (IDs 22457 and 28846), however, do not separate from the star-forming galaxies in any of the optical diagnostics; these do not appear to be AGN in the BPT diagram. We therefore conclude that at least two or three of the six optical AGN candidates are very likely to be AGN, based on multiple optical diagnostics. The complete MOSDEF sample will be useful to re-examine the Kauffmann et al. (2003) and Meléndez et al. (2014) lines and their applicability at $z \sim 2$ and will allow us to further determine optical AGN demographics at $z \sim 2$.

4.2. *Completeness of the BPT Diagram for AGN Identification*

In this section we discuss the completeness of optical AGN identification using the BPT diagram, both at low and high redshift.

It should first be mentioned that when creating optically-selected AGN samples using the BPT diagram, "composite" sources should be included when one is interested in having a more complete AGN sample. While some of the line emission in these sources is from star formation, the line ratios indicate that ionization from AGN is also present, such that samples that exclude these sources will be incomplete. In the SDSS, 35% of SDSS sources that have all four lines required for the BPT diagram detected are classified as AGN when including "composite" sources. This fraction decreases to 13% when using only sources above the Kewley et al. (2001) line, which are defined such that there is no con-

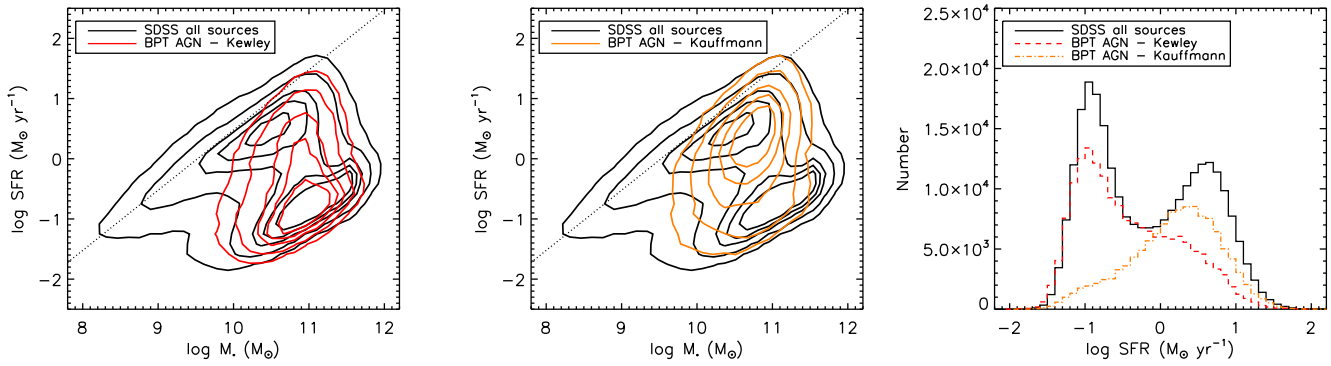

FIG. 8.— Left: Star formation rate versus stellar mass for all SDSS DR7 sources (black contours) and SDSS AGN (red contours), defined as sources above the Kewley et al. (2001) line in the BPT diagram. The dotted black line indicates a constant log (sSFR/yr^{-1}) = -9.5. Middle: Black contours are the same as in the left panel, with orange contours showing "composite" sources between the Kauffmann et al. (2003) and Kewley et al. (2001) lines in the BPT diagram. Right: Star formation rate distribution for sources with $10.5 < \log (M_*/M_\odot) < 11$ for all SDSS sources (black), AGN above the Kewley et al. (2001) line (red, scaled up by a factor of 7), and "composite" sources (orange, scaled up by a factor of 3). AGN identified using the Kewley et al. (2001) line are preferentially in quiescent galaxies, while "composite" sources identified using the Kauffmann et al. (2003) line are preferentially in star-forming galaxies. Both AGN selections have a bias against identifying AGN in low mass galaxies.

tribution to the line ratios from star formation. This relatively high fraction, especially when including composite sources, indicates that, at least in SDSS, AGN can be identified down to low Eddington ratios using the BPT diagram (Aird et al. 2012; Kelly & Shen 2013).

Alternatively, the BPT diagram can be used to identify AGN that one wishes to exclude as "contaminants" in samples of star-forming galaxies. We find that the BPT diagram can be used in such a manner at $z \sim 2$, as moderate-luminosity ($\log (L_X/(\mathrm{erg\ s^{-1}})) > 43$) X-ray and IR AGN do separate fairly cleanly in the BPT diagram from star-forming galaxies at these redshifts. However, using the BPT diagram in this way (even including "composite" sources using the local Kauffmann et al. (2003) line) will not identify *all* AGN, as the BPT diagram has biases and is incomplete in terms of AGN selection, as is any AGN selection technique.

Identifying complete AGN samples requires multi-wavelength data and AGN selection across a range of wavebands. Optical AGN selection, using the BPT diagram, should in theory be somewhat complementary to selections at other wavelengths, as it should identify both lower luminosity and/or more obscured AGN. It should also be useful if there is little or only shallow X-ray data of the sources of interest. Additionally, as X-ray imaging is subject to substantial vignetting, resulting in a non-uniform depth across a field, optical AGN identification could be useful to ensure a more uniform selection as a function of depth and could identify AGN that are missed when the X-ray data is "off-axis".

However, optical AGN identification has selection effects that must be taken into account. One may expect a bias against identifying AGN in galaxies with high specific star formation rates, as the line ratios in such galaxies may be dominated by star formation. In the BPT diagram AGN will likely be more easily identified if they reside in galaxies with less star formation, where Hα and Hβ are low. There is therefore a selection bias towards identifying AGN in galaxies with older stellar populations. Additionally, the presence of dust can preferentially extinguish [O III] produced by the AGN, such that the BPT diagram is biased against identifying AGN in very dusty galaxies (Goulding & Alexander 2009).

These selection biases are shown in Fig. 8, where we show in black contours the SFRs and stellar masses of all SDSS DR7 sources, while in red contours (left panel) we show the distribution for those sources identified as AGN in the BPT diagram, using the Kewley et al. (2001) line (see also Salim et al. 2007). The middle panel shows the distribution of "composite" sources (orange contours) identified using the Kauffmann et al. (2003) line, and the right panel shows the distribution of star formation rates for AGN and all sources with $10.5 < \log (M_*/M_\odot) < 11$. The Kewley et al. (2001) selection clearly preferentially identifies AGN in quiescent galaxies. While almost no AGN are identified in sources with high specific star formation rate (sSFR = SFR/M$_*$), as shown by the dotted line in the left panel, there are also relatively few star-forming hosts for these AGN, as shown in the right panel. The Kauffmann et al. (2003) selection preferentially identifies AGN in star-forming hosts, though even among the star-forming hosts the median star formation rate is lower for the identified AGN hosts than for the full galaxy population.

While this figure alone does not fully indicate whether these differences in galaxy properties are intrinsic to AGN hosts or are due to selection effects, when these results are compared with the literature it is clear that there are strong selection effects at play. A number of recent studies have indicated that X-ray selected AGN at intermediate and high redshift are in fact preferentially hosted by star-forming galaxies. Rovilos et al. (2012) used Herschel data to show that X-ray selected AGN in the CDFS (spanning $z \approx 0.5 - 4$) are mostly hosted by galaxies with similar (or higher) sSFRs as typical star-forming galaxies at the same redshift. Rosario et al. (2013) and Harrison et al. (2012) both measured average SFRs of X-ray selected AGN in the COSMOS, GOODS and GOODS-N fields by stacking *Herschel* data and found that the average SFRs were consistent with normal star-forming galaxies at the same redshift. Furthermore, Mullaney et al. (2012) and Santini et al. (2012) showed that X-ray AGN have high detection rates in the far-IR, which indicates that the majority are hosted by nor-

mal star-forming galaxies. Most recently, Azadi et al. (2014) showed that the probability of a galaxy hosting an X-ray selected AGN above a given Eddington ratio is higher for star-forming galaxies than quiescent galaxies and generally increases with sSFR (they also showed that the Eddington ratio distribution does not change with stellar mass or SFR at 0.2 ¡ z ¡ 1.2). Taken together, these results have shown that AGN commonly reside in star-forming galaxies with relatively high SFRs, while we show above that the BPT diagram, even when including composite sources, has a bias against identifying AGN in such galaxies.

Fig. 8 also clearly shows a strong selection effect with stellar mass. This is a known selection effect whereby AGN are more easily detected in massive host galaxies, which have more massive black holes that can therefore been seen down to lower Eddington ratios (Aird et al. 2012). This stellar mass bias exists at all redshifts for flux-limited samples, regardless of the waveband used to identify AGN (e.g., Hainline et al. 2009). In the BPT diagram, AGN are most likely to be identified in massive galaxies, which on average have higher metallicities (i.e., Tremonti et al. 2004) and therefore higher [N II]/Hα ratios. The presence of an AGN boosts the [N II]/Hα ratio further, such that AGN fall to the right in the BPT diagram. It is therefore quite difficult to detect AGN in low mass (and low metallicity) host galaxies using the BPT diagram (Groves et al. 2006; Stasińska et al. 2006). In fact, Aird et al. (2013) suggest that AGN do exist in low mass galaxies, but a flux-limited AGN sample will necessarily be dominated by massive host galaxies (where it is easier to identify an AGN down to a lower Eddington ratio compared to lower mass galaxies), such that low mass AGN hosts will be fairly rare in flux-limited samples.

The issue of completeness of the BPT diagram for AGN selection becomes much worse at high redshift, where there are fewer quiescent galaxies than at $z \sim 0$ (e.g., Ilbert et al. 2013; Muzzin et al. 2013). Additionally, SFRs at a given stellar mass are generally higher at high redshift (e.g., Pannella et al. 2009; Elbaz et al. 2011; Karim et al. 2011; Whitaker et al. 2012), such that it will likely be harder to identify AGN in the BPT diagram at high redshift, as the line fluxes will have more contribution from star formation. While the global AGN accretion rate is also higher at high redshift, and generally traces the evolution in the global SFR well, in order to identify AGN in the BPT diagram the host galaxy must have a low sSFR. As only AGN in galaxies with relatively low sSFR and high stellar mass can be identified using the BPT diagram, at high redshift this will be a more severe incompleteness than at low redshift, due to the relative dearth of massive galaxies with older stellar populations, when compared to low redshift. Indeed, in MOSDEF the X-ray and IR AGN have lower sSFR (as derived from SED fits) than the bulk of the galaxy sample (see also Kriek et al. 2007).

The result is that the BPT diagram works well in SDSS, due to the selection effect of identifying AGN in massive galaxies, which at low redshift are often quiescent. This allows the AGN to contribute substantially to the line ratios in the BPT diagram, such that the detected AGN clearly separate in this space. At high redshift, however, massive galaxies are not as likely to be quiescent and SFRs are higher, such that it is harder for AGN to cleanly separate in the BPT diagram.

Indeed, we find here that there is substantial overlap between X-ray/IR AGN and candidate optical AGN identification at $z \sim 2$, in that in the BPT diagram the X-ray/IR AGN all lie above the Kauffmann et al. (2003) and Meléndez et al. (2014) lines. It appears that optical selection, using the BPT diagram, provides a ≈50% more complete AGN sample than X-ray and IR selection.

4.3. *Completeness of the MEx Diagram for AGN Identification*

While reliance on the MEx diagram is becoming less neccessary at $1 < z < 3$, given the new multi-object NIR spectrographs that can observe [O III]/Hβ and [N II]/Hα at these redshifts, this diagnostic is currently used. Can the MEx diagram be used at these redshifts to reliably identify AGN?

Juneau et al. (2014) argue that it can, as long as the line luminosity limits and redshift of the sample are taken into account. They show that in SDSS while the demarcations between star-forming galaxies and AGN in the BPT diagram do not change as the line luminosity limit of a sample is decreased, shallower surveys will miss galaxies or AGN with low [O III]/Hβ, such that the lower part of the BPT diagram will not be occupied. This results in a shift in the AGN classification lines in the MEx diagram to higher stellar mass.

One way to understand this shift is that flux-limited surveys at any wavelength are biased towards identifying AGN with high host stellar masses (Aird et al. 2012), as more massive galaxies host more massive SMBHs, which can be identified to a lower Eddington ratio (at a given flux limit) than SMBHs in lower mass galaxies. Therefore shallower surveys will mainly find AGN in more massive galaxies. In less massive galaxies, only the (rare) AGN with high Eddington ratio will be detected. The detected AGN population will therefore be dominated by those with higher stellar mass host galaxies, and thus the AGN classification lines are shifted to higher stellar mass as the line luminosity limits increase.

Juneau et al. (2014) include an additional shift due to evolution in L^* of both Hα and [O III]. This reflects that a given luminosity limit does not probe as far down the luminosity function at low redshift as it does at high redshift, given that L^* is lower at low redshift. To select galaxies to the same relative depth on the luminosity function, one therefore has to reduce the luminosity limit at low redshift, which reduces the stellar mass shift in the MEx diagram at high redshift.

We find here that for our MOSDEF sample, the shift to higher stellar mass proposed by Juneau et al. (2014) is insufficient to cleanly separate known AGN from the rest of the sample. Additionally, Domínguez et al. (2013) show that galaxies at $0.75 < z < 1.5$ with high $L_{H\alpha}$ do not also have high [O III]/Hβ, as in SDSS. We find that a stellar mass shift that takes into account the evolution in the mass-metallicity relation of galaxies (in that at a given stellar mass galaxies have lower metallicity and higher [O III]/Hβ at high redshift) is required to cleanly separate star-forming galaxies and AGN in the MEx diagram at $z \sim 2.3$. The need for a shift in the MEx diagram with redshift may be evolution in the mass-metallicity relation, rather than the evolution of L_* and the depth of a survey.

TABLE 4
AGN Optical Classification Comparison

Diagnostic	X-ray/IR AGN [a]	Identified as AGN [b]	Not Identified as AGN	Potential Contaminants [c]	Likely Additional Optical AGN [d]
BPT - Kewley et al. (2013a)	9	5	4	2	2
BPT - Kauffmann et al. (2003)	9	9	0	6	4
BPT - Melendez et al. (2014)	9	9	0	4	4
MEx - Juneau et al. (2014)	10	9	1	34	2
MEx - this paper	10	6	4	4	1
CEx - Yan et al. (2011)	9	6	3	12	1
CEx - Trump et al. (2013)	9	6	3	36	4

[a] The number of AGN defined *a priori* by X-ray and/or IR emission.
[b] The number of *a priori* AGN positively identified as AGN using this optical diagnostic.
[c] The number of MOSDEF sources that were not identified *a priori* as X-ray/IR AGN that are identified as optical AGN using this diagnostic. These are potential contaminants as they could be star-forming galaxies.
[d] The number of potential contaminants that likley are AGN, given their location in the BPT diagram.

We find that the MEx diagram at $z \sim 2$ is fairly complete in terms of identifying X-ray/IR-selected AGN, but it does not identify most of the candidate BPT "composite" sources, i.e. those sources that might be AGN based on their location in the BPT diagram. As shown above, it may additionally suffer from contamination by star-forming galaxies in the "composite" region of the MEx diagram, though this is alleviated somewhat by the probabilistic AGN classification of Juneau et al. (2014). Given this, we propose that the full BPT diagram should be used to identify optical AGN samples at $z \sim 2$.

4.4. *Comparison of Completess and Contamination of Optical AGN Diagnostics*

In this section we compare the various optical AGN diagnostics presented in this paper and discuss the completeness and potential contamination of each. Table 4 lists the three optical diagnostics, along with the various proposed classification lines in each diagnostic, along with the number of AGN defined *a priori* by X-ray and/or IR emission that can be used for each diagnostic, the number of those AGN that are positively identified as optical AGN (for AGN ID 6, we count it as identified if at least one of the two spectral components is identified), the corresponding number of X-ray/IR AGN that are missed (i.e., not positively identified as AGN), and the number of MOSDEF sources that are not X-ray/IR AGN (i.e., galaxies) that are identified as optical AGN using that diagnostic. The latter are potential contaminants, as they could be star-forming galaxies and not AGN. Finally, the last column indicates the number of those potential contaminants that are likely to be AGN, given their location in the BPT diagram. Here a source has to clearly be in the AGN wing of the BPT diagram and have a high [N II]/Hα ratio ($\log > -0.4$) and/or be above the Kewley et al. (2013b) line to be a likely optical AGN. It is possible that additional potential contaminants are AGN, but we can not know without BPT classifications for all of the sources (i.e., those with S/N<3 in [N II]/Hα) and/or deeper X-ray data.

Our initial MOSDEF sample is small, and thus the errors on the completeness and contamination presented here are large. We will revisit these issues with the full dataset, however with our current sample we find that of the three BPT classification lines presented, the Meléndez et al. (2014) line is both the most complete—identifying all nine of the *a priori* X-ray/IR AGN and four additional sources that are very likely to be AGN—and the least contaminated (in that all of the four potential contaminants are very likely to be AGN). While the Kewley et al. (2013b) line is not likely to be contaminated, it is not as complete, only identifying five of the nine *a priori* AGN, along with two further likely optical AGN. The Kauffmann et al. (2003) line does identify all nine of the *a priori* AGN but is likely somewhat contaminated (as two of the six additional sources identified with this diagnostic are likely to be star-forming galaxies without significant AGN contributions).

As presented earlier, the classification lines in the MEx diagram from Juneau et al. (2014) lead to substantial contamination; we therefore propose a larger shift in these lines to minimize this contamination. However, this reflects in a lower fraction of X-ray/IR AGN being positively identified, and there is still some contamination, as the four additional galaxies that are classified as AGN are *not* classified as AGN in the BPT diagram. Since the MEx classification lines were originally defined by BPT classifications such that only those sources that are AGN in the BPT diagram can be AGN in the MEx diagram, it appears that even with the shifted classification lines proposed here, there is still some contamination. Finally, the CEx classifications are highly contaminated, using either the orginal line proposed by Yan et al. (2011) or the revised line of Trump et al. (2013).

4.5. *Metallicities of $z \sim 2$ AGN*

Kewley et al. (2013a) present predictions for the locations of galaxies and AGN in the BPT diagram at high redshift, depending on the physical conditions in the ISM of galaxies and the metallicity of gas near the AGN. They present two predictions for the locations of star-forming galaxies: one is identical to the location of star-forming galaxies at $z \sim 0$, if the ISM conditions in high-redshift galaxies match those found locally. The other scenario shows the positions of galaxies that have "extreme" ISM conditions, which could be due to a larger ionization parameter and a more dense ISM, and/or a harder ionizing radiation field. They also have two predictions for the locations of AGN in the BPT diagram: in one scenario the gas near the AGN is enriched to a higher metallicity than is found generally in the host galaxy ("metal-rich" AGN) and in the other scenario the gas near the AGN

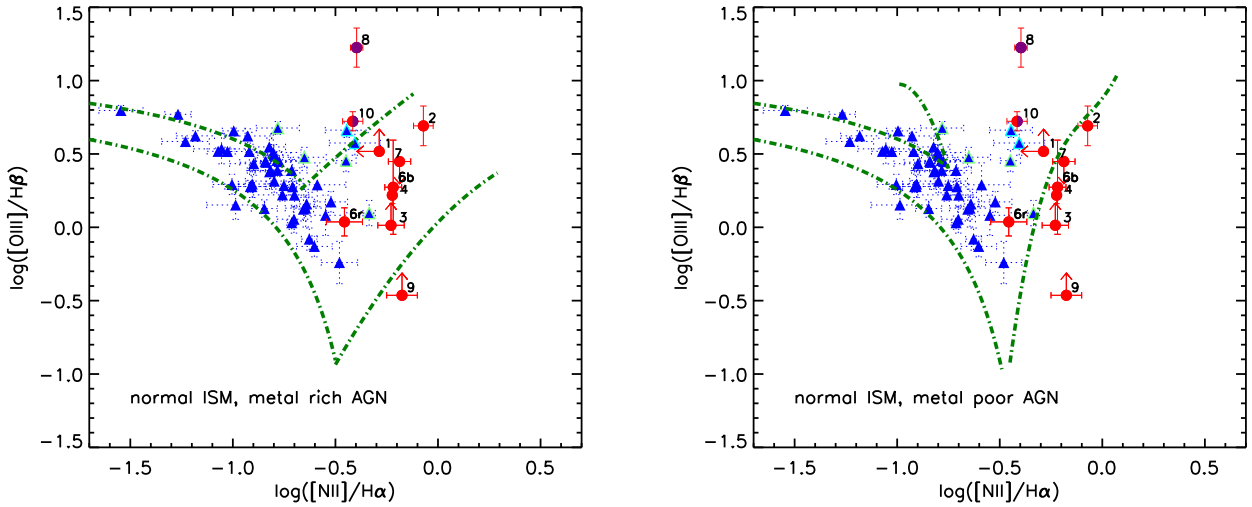

FIG. 9.— Same as Fig. 3 but here the dark green dot-dashed lines show the predicted locations of star-forming galaxies and AGN at $z = 2.5$ for the two scenarios presented in Kewley et al. (2013a) with "normal" or local ISM conditions. The left panel shows predictions for metal-enriched AGN, where the gas near the AGN is enriched relative to the host galaxy, while the right panel shows those for metal-poor AGN, where the gas near the AGN has a similar metallicity as the gas in the host galaxy.

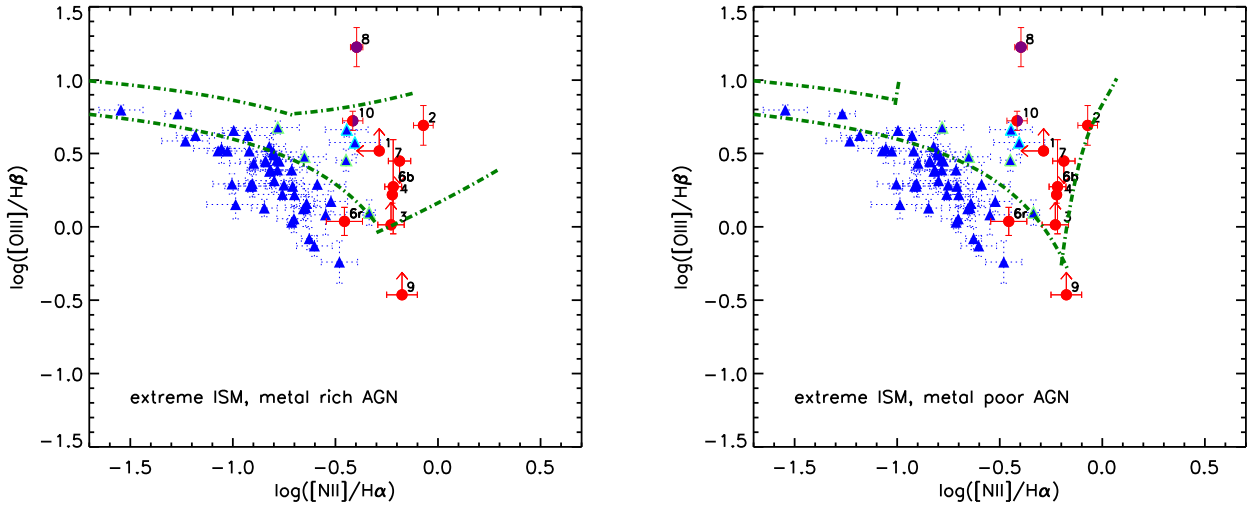

FIG. 10.— Same as Fig.3 but here the dark green dot-dashed lines show the predicted locations of star-forming galaxies and AGN at $z = 2.5$ for the two scenarios presented in Kewley et al. (2013a) with "extreme" ISM conditions. As in Fig. 9, the left panel shows predictions for metal-enriched AGN, while the right panel for metal-poor AGN.

has the same metallcity as the gas in the host galaxy, on larger scales ("metal-poor" AGN).

In Figs. 9 and 10 we compare the locations of MOSDEF galaxies and AGN at $z \sim 2.3$ with these predictions. Fig. 9 corresponds to their scenarios 1 and 2, where "local" ISM conditions prevail at high redshift, with the left panel showing the location of metal-rich AGN and the right panel showing the location of metal-poor AGN. Fig. 10 corresponds to their scenarios 3 and 4, where "extreme" ISM conditions prevail at high redshift, and again the left panel shows metal-rich AGN and the right panel metal-poor AGN.

We find that at $z \sim 2$ local ISM conditions do not appear to match the local star-forming sequence perfectly, in that in Fig. 9 the MOSDEF galaxies have a higher [O III]/Hβ and/or [N II]/Hα than predicted (see also Shapley et al. 2014) But the difference is not large. Fig. 10 clearly shows that the "extreme" ISM conditions presented in Kewley et al. (2013a) are too extreme, as most MOSDEF galaxies lie well below the star-forming sequence. Overall, the data may prefer a somewhat intermediate ISM, though the local ISM conditions appear to work reasonably well.

In terms of the location of MOSDEF AGN, for the "normal" ISM models (Fig. 9) they do not appear to be particularly metal poor, in that six of the ten AGN have [N II]/Hα ratios greater than the "metal-poor" prediction. The bulk of the AGN sample (seven out of ten sources) lies within the "metal-rich" predictions. Alternatively, at least four AGN have higher [N II]/Hα than the "metal-poor" prediction. But many of the MOSDEF AGN fall in the overlapping regions of the "metal-rich" and "metal-poor" predictions, such that their locations are not conclusive. It appears that according to these

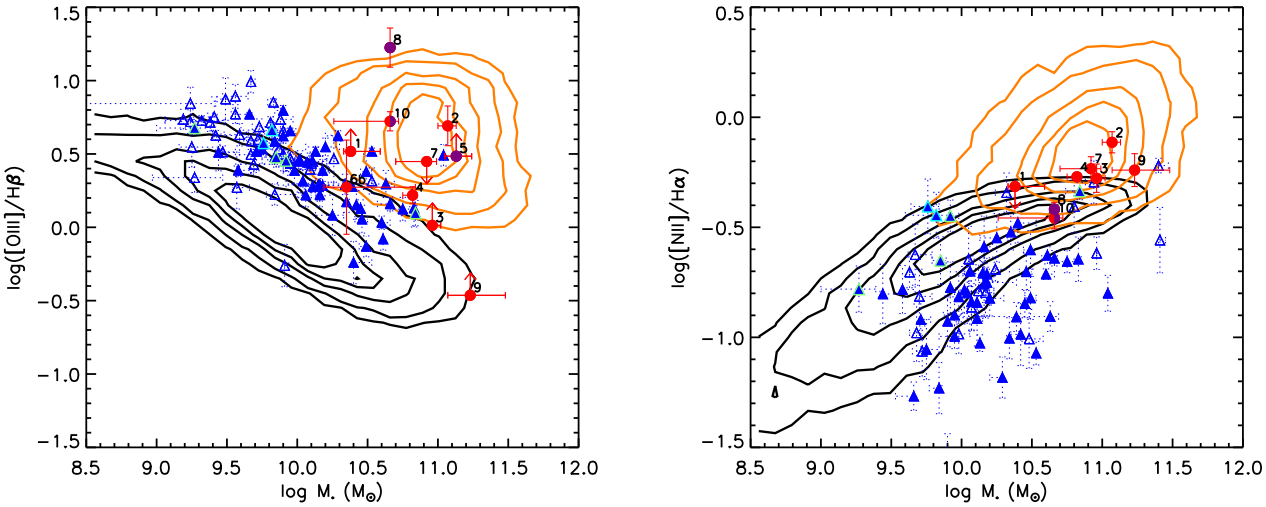

FIG. 11.— A comparison of the [O III]/Hβ and [N II]/Hα ratios of MOSDEF galaxies (blue triangle) and AGN (red circles) as a function of stellar mass, compared to galaxies (black contours) and AGN (orange contours) in SDSS. The left diagram is the MEx diagram of Fig. 5, where here we have split the SDSS comparison sample based on location in the BPT diagram; orange contours show SDSS sources above the Kauffmann et al. (2003) line in the BPT diagram. Open blue triangles show galaxies that are not included in Fig. 3, due to low S/N in [N II] and/or Hα (left panel) or [O III] and/or Hβ (right panel).

models at least some AGN at $z \sim 2$ are "metal-rich", in that the metallicity of the gas in the narrow-line region is higher than that in the host galaxy on larger scales.

To investigate further the metallicity evolution of the AGN, we show in Fig. 11 the [O III]/Hβ and [N II]/Hα ratios of galaxies and AGN as a function of stellar mass in both MOSDEF and SDSS. Here SDSS sources are shown only if they are above the line luminosity limits of MOSDEF. The left panel is the MEx diagram, while the right panel reflects the mass-metallicity relation in both MOSDEF and SDSS (Tremonti et al. 2004; Sanders et al. 2014). We show SDSS AGN identified using the Kauffmann et al. (2003) line with orange contours, as it is likely that the line ratios are impacted for all of "composite" AGN as well as AGN above the Kewley et al. (2001) line.

In general, the range of [O III]/Hβ that is observed reflects both the AGN accretion rate (which will be higher for AGN with higher [O III]) and the age of the stellar population. [N II]/Hα reflects the metallicity of the host galaxy and has an additional contribution to the flux of the [N II] line from the ionizing radiation from the AGN. As discussed above, the appearance of the AGN wing in the BPT diagram is due to a combination of the AGN ionizing radiation and the high stellar mass of the host galaxy. Indeed, the fact that the MEx diagram works well for AGN in SDSS reflects that the AGN region of the BPT diagram really just depends on AGN luminosity (in both [O III] and [N II]) and host stellar mass (in [N II]/Hα).

The fact that we see in Fig. 11 that MOSDEF AGN have lower [N II]/Hα ratios than AGN in SDSS with the same host galaxy stellar mass, on average, indicates that the narrow-line region of AGN at $z \sim 2$ are less enriched than those at $z \sim 0$, at a given host stellar mass. It is also unlikely that the gas in the narrow-line region is strongly enriched compared to the host galaxy; otherwise the [N II]/Hα ratio for the AGN would be even higher, given the additional contribution to [N II] from the AGN.

The left panel of this figure also indicates that the presence of an AGN boosts the [O III] line luminosity more so than the [N II] line luminosity, in that both SDSS and MOSDEF AGN have higher [O III]/Hβ ratios than galaxies of a similar stellar mass, while the [N II]/Hα ratios for AGN are not nearly as elevated compared to galaxies of the same stellar mass. Indeed, the [O III]/Hβ ratios of MOSDEF AGN generally span the range observed for SDSS AGN, which likely means that the [O III]/Hβ ratio for AGN is particularly sensitive to the AGN accretion rate and not as sensitive to host galaxy properties, unlike the [N II]/Hα ratio. We conclude then that while the gas in the narrow-line region at $z \sim 2$ may be somewhat more enriched than the gas further out in the host galaxy, the narrow-line regions of AGN at $z \sim 2$ are not as enriched, at a given host galaxy stellar mass, as in the local universe.

We note that for the right panel of Fig. 11 we show all MOSDEF sources that have S/N $>$ 3 for either of the [N II] or Hα lines, regardless of the S/N of the [O III] or Hβ lines. This results in a sample of 68 galaxies, somewhat larger the sample shown in Fig. 3. We find for this larger sample that there are three additional galaxies with AGN-like [N II]/Hαline ratios; in the BPT diagram most MOSDEF X-ray and IR AGN have log ([N II]/Hα)$\gtrsim -0.4$, roughly corresponding to the location of the Kauffmann et al. (2003) line for the MOSDEF sources with the lowest measured [O III]/Hβ values. In the larger MOSDEF galaxy sample shown here, there are a total of two galaxies with [N II]/H$\alpha$$> -0.25$ and five galaxies with [N II]/H$\alpha$$> -0.35$. Two of these sources have robust [O III]/Hβ ratios such that they were already highlighted in Fig. 3 with light green outlines (with log ([O III]/Hβ) values of -0.11 and -0.34); the rest have a night sky line at the location of Hβ. The source information for these three new optically-identified AGN candidates is given in Table 3. Of these three sources, one is very likely to be an AGN, given the measured [N II]/Hα value of -0.22. Of the potential "composite"

sources (shown with light green outlines), the two with high [N II]/Hα ratios appear to be AGN from this figure (and indeed from the BPT diagram, as discussed above). The other three sources have lower stellar masses and [N II]/Hα values near the upper range for their mass. Indeed, one source is near the two cyan points, which are above the Kewley et al. (2013b) line in the BPT diagram, and could be an AGN.

We emphasize again, however, that the AGN incidence in the MOSDEF sample can not be calculated by simply taking the ratio of the sources with AGN-like line ratios to the full galaxy sample, as one must take into account the targeting weights. Such an analysis will be presented in a future paper.

4.6. *Are Weak AGN Contaminating the BPT Diagram at High Redshift?*

It has been suggested that contamination from weak AGN is causing the "offset" seen for star-forming galaxies in the BPT diagram. Wright et al. (2010) argue from the spatial distributions of [O III]/Hβ and [N II]/Hα for a single source at $z = 1.6$ with OSIRIS data that weak AGN contribution can shift the location of a star-forming galaxy in the BPT diagram to the AGN region. Of course while this is possible for individual sources, requiring the entire "offset" observed in the BPT diagram for galaxies at high redshift to be due entirely to AGN without increasing the width of the star-forming sequence would require most high-redshift galaxies to have at least weak AGN. As discussed above, at high redshift it is even harder to identify lower luminosity AGN in the BPT diagram, compared to SDSS, so this is likely not the answer. Additionally, given that star formation rates are generally higher at high redshift, a weak AGN would likely have a lower contrast with the star formation in the host galaxy and therefore not impact the emission line ratios as substantially in the BPT diagram. Indeed for the source in Wright et al. (2010), the high [O III]/Hβ and [N II]/Hα ratios do not appear to be spatially coincident with the center of the galaxy, as defined in Hα, and could potentially be due to shocks (i.e., Kewley et al. 2013b). For this source it might be useful to measure the [S II]/Hα ratio to look for LINER and/or shock emission.

Trump et al. (2011) use *HST*/WFC3 grism spectroscopy of 28 galaxies at $z \sim 2$ to measure the spatial extent of the [O III] and Hβ emission lines in stacked spectra of their full sample. They find at the $\sim 2.5\sigma$ level that the [O III] emission is more centrally concentrated than the Hβ emission, and further find that stacked X-ray emission of all of their sources shows signatures of at least some AGN emission. It is possible again that the more concentrated [O III] profile could have some contribution from shocks, however it is more likely that they have a few AGN in their sample contributing to their stacked results. Indeed, in a CEx diagram two of their sources are very red and have high [O III]/Hβ, putting them in the local AGN region. The presence of two AGN would account for their results, without implying detections of AGN in low mass, low metallicity galaxies, which seems very unlikely given the selection effects discussion above.

Interestingly, Steidel et al. (2014) find that their sample of $z \sim 2$ galaxies is substantially offset in the BPT diagram, and their sample only contains a handful of known AGN, from UV spectral lines. Jones et al. (2013) also find offsets in the BPT diagram for spatially-resolved lensed galaxies with no known AGN contribution; they find that star-forming regions of all radii in their galaxies are offset. As shown here in Section 4.1, some of the observed offset in the BPT diagram for high redshift galaxies is alleviated by comparing with local samples with similar line luminosity limits (Juneau et al. 2014). There is a small ($\sim$0.1 dex) residual offset even after such selection effects are taken into account, which could in theory be due to changes in e.g., the ionization parameter at high redshift (e.g., Kewley et al. 2013a; Steidel et al. 2014).

As discussed above in Section 4.2, while it is known that there is greater AGN activity at high redshift, there is a similar increase in star formation, such that it is unlikely that an increase in AGN activity could substantially move galaxies in the BPT diagram from the star forming sequence towards the AGN region. More importantly, there are additional stellar mass and stellar population selection effects, such that it is easier to identify AGN in the BPT diagram in massive, quiescent galaxies. Given that galaxies at high redshift have younger stellar populations, on the whole, it appears very unlikely that the line ratios for galaxies in the star forming sequence in the BPT diagram at high redshift can be substantially impacted by AGN activity. Indeed, we have shown that at high redshift the BPT diagram should identify *fewer* AGN than at low redshift, as only high luminosity AGN (or shocks) can substantially impact the line ratios and move sources to the AGN region of the diagram. In Newman et al. (2014), only those $z \sim 2$ sources above the Kewley et al. (2001) line have a shift to higher line ratios in the BPT diagram using spatially-resolved line ratios. This result is consistent with AGN contamination from weak AGN (which are likely not above the Kewley et al. (2001) line) not contributing substantially to the BPT offset for galaxy samples. As discussed in Shapley et al. (2014) the offset of high-redshift galaxies in the BPT diagram appears to be due instead to lower mass galaxies ($M_* < 10^{10}$ $M_\odot$) at these redshift having elevated N/O ratios (see also Masters et al. 2014; Steidel et al. 2014).

5. CONCLUSIONS

Using MOSFIRE data for $\sim$ 50 galaxies and 10 X-ray and IR-selected AGN at $z \sim 2.3$ from the first season of the MOSDEF survey, we investigate the identification and completeness of optical AGN diagnostics at $z \sim 2$. We present the location of X-ray and IR-selected AGN in the BPT, MEx, and CEx diagrams for our sample and compare with BPT-identified AGN in SDSS. Our main conclusions are as follows:

- Measurements of [N II]/Hα are required to optically-identify AGN at $z \sim 2$, as AGN have a wide range of [O III]/Hβ values that overlaps the $z \sim 2$ galaxy population, such that [O III]/Hβ alone is insufficient to identify AGN. It may even be possible to use [N II]/Hα alone to identify AGN in the MOSDEF sample, given that the [O III]/Hβ ratios are uniformly high.
- The BPT diagram works well at $z \sim 2$, in that X-ray and IR-selected AGN separate cleanly from

the star-forming galaxy population in the MOSDEF sample. The $z \sim 0$ AGN/star-forming galaxy classifications appear to need to shift by only $\sim 0.1 - 0.2$ dex at $z \sim 2$ to robustly separate these populations. The new Meléndez et al. (2014) classification also appears to work well at $z \sim 2$.

- The MEx diagram does not appear to work as well at $z \sim 2$, in that the classification lines at $z \sim 0$ need to be shifted substantially at high redshift, more so than predicted in the literature (Juneau et al. 2014). Additionally, the MEx diagram fails to identify some of the optical AGN candidates identified by the BPT diagram. The CEx diagram can not be used at $z \sim 2$, as there is not a simple shift in the CEx classification line that would cleanly separate star-forming galaxies and AGN at these redshifts. We conclude that it is preferable to use the BPT diagram for optical AGN selection at high redshift.

- AGN identification using the BPT diagram is subject to selection biases, in that AGN are easier to detect in the BPT diagram if they reside in massive and/or quiescent host galaxies. While this is true at both low and high redshift, these selection biases become stronger at high redshift where massive galaxies show a larger diversity in color and star formation rate.

- While AGN identification using the BPT diagram can not provide a complete AGN sample, it can be used to identify a "pure" AGN sample with little contamination from star-forming galaxies. However, AGN identification using the BPT diagram will be incomplete if only sources above the Kewley et al. (2001) line are classified as AGN. Therefore one should include BPT "composite" sources when creating more complete AGN samples. An updated classification line for "composite" sources at $z \sim 2$ will require the full MOSDEF sample, though the Meléndez et al. (2014) classification may work well for this purpose.

- Contamination from AGN can not be shifting the bulk of the galaxy population at high-redshift to the AGN region of the BPT diagram, causing the observed offset in the galaxy population.

- In at least some MOSDEF AGN, the gas in the narrow-line region appears to be more enriched than gas in the host galaxy. Overall, however, AGN at $z \sim 2$ are less enriched than local AGN with the same host stellar mass.

With data from the first observing season of the MOSDEF survey, we have demonstrated the power of the survey for AGN studies. As the sample size increases we will further study the demographics and host galaxy properties of optical versus X-ray and IR-selected AGN, as well as the X-ray emission of MOSDEF galaxies as a function of key galaxy physical properties such as stellar mass, SFR, stellar age, and metallicity.

We thank the MOSFIRE instrument team for building this powerful instrument, and for taking data for us during their commissioning runs. We are also grateful to Marc Kassis for his many valuable contributions to the execution of our survey. This work would not have been possible without the 3D-HST collaboration, who provided us the spectroscopic and photometric catalogs used to select our targets and to derive stellar population parameters. Based on observations made with the NASA/ESA Hubble Space Telescope, which is operated by the Association of Universities for Research in Astronomy, Inc., under NASA contract NAS 5-26555. These observations are associated with programs 12177, 12328, 12060-12064, 12440-12445, 13056. Funding for the MOSDEF survey is provided by NSF AAG grants AST-1312780, 1312547, 1312764, and 1313171 and grant AR-13907 from the Space Telescope Science Institute. ALC acknowledges support from NSF CAREER award AST-1055081. NAR is supported by an Alfred P. Sloan Research Fellowship. ALC thanks the Aspen Center for Physics for providing a quiet location at which to write parts of this manuscript. The data presented herein were obtained at the W.M. Keck Observatory, which is operated as a scientific partnership among the California Institute of Technology, the University of California and the National Aeronautics and Space Administration. The Observatory was made possible by the generous financial support of the W.M. Keck Foundation. The authors wish to recognize and acknowledge the very significant cultural role and reverence that the summit of Mauna Kea has always had within the indigenous Hawaiian community. We are most fortunate to have the opportunity to conduct observations from this mountain.

REFERENCES

Aird, J., et al. 2010, MNRAS, 401, 2531
—. 2012, ApJ, 746, 90
—. 2013, ApJ, 775, 41
Alonso-Herrero, A., Pérez-González, P. G., Alexander, D. M., et al. 2006, ApJ, 640, 167
Ashby, M. L. N., et al. 2013, ApJ, 769, 80
Azadi, M., et al. 2014, ArXiv 1407.1975
Baldwin, J. A., Phillips, M. M., & Terlevich, R. 1981, PASP, 93, 5
Barger, A. J., Cowie, L. L., Mushotzky, R. F., et al. 2005, AJ, 129, 578
Barmby, P., Huang, J.-S., Ashby, M. L. N., et al. 2008, ApJS, 177, 431
Barro, G., Faber, S. M., Pérez-González, P. G., et al. 2013, ApJ, 765, 104
Bongiorno, A., Merloni, A., Brusa, M., et al. 2012, MNRAS, 427, 3103
Boyle, B. J., Griffiths, R. E., Shanks, T., Stewart, G. C., & Georgantopoulos, I. 1993, MNRAS, 260, 49
Boyle, B. J., & Terlevich, R. J. 1998, MNRAS, 293, L49
Brammer, G. B., Whitaker, K. E., van Dokkum, P. G., et al. 2011, ApJ, 739, 24
Brammer, G. B., et al. 2012, ApJS, 200, 13
Brusa, M., Civano, F., Comastri, A., et al. 2010, ApJ, 716, 348
Brusa, M., et al. 2007, ApJS, 172, 353
Bruzual, G., & Charlot, S. 2003, MNRAS, 344, 1000
Chabrier, G. 2003, PASP, 115, 763
Ciliegi, P., et al. 2003, A&A, 398, 901
—. 2005, A&A, 441, 879

Cimatti, A., et al. 2013, ApJ, 779, L13
Conroy, C., Gunn, J. E., & White, M. 2009, ApJ, 699, 486
Delvecchio, I., et al. 2014, MNRAS, 439, 2736
Domínguez, A., Siana, B., Henry, A. L., et al. 2013, ApJ, 763, 145
Donley, J. L., Rieke, G. H., Rigby, J. R., & Pérez-González, P. G. 2005, ApJ, 634, 169
Donley, J. L., et al. 2012, ApJ, 748, 142
Elbaz, D., Dickinson, M., Hwang, H. S., et al. 2011, A&A, 533, A119
Elvis, M., Wilkes, B. J., McDowell, J. C., et al. 1994, ApJS, 95, 1
Erb, D. K., Shapley, A. E., Pettini, M., Steidel, C. C., Reddy, N. A., & Adelberger, K. L. 2006, ApJ, 644, 813
Fazio, G. G., Hora, J. L., Allen, L. E., et al. 2004, ApJS, 154, 10
Georgakakis, A., et al. 2014, MNRAS, 440, 339
Giavalisco, M., Ferguson, H. C., Koekemoer, A. M., et al. 2004, ApJ, 600, L93
Gilli, R., Comastri, A., & Hasinger, G. 2007, A&A, 463, 79
Goulding, A. D., & Alexander, D. M. 2009, MNRAS, 398, 1165
Grogin, N. A., Kocevski, D. D., Faber, S. M., et al. 2011, ApJS, 197, 35
Groves, B. A., Heckman, T. M., & Kauffmann, G. 2006, MNRAS, 371, 1559
Hainline, K. N., Shapley, A. E., Greene, J. E., et al. 2012, ApJ, 760, 74
Hainline, K. N., Shapley, A. E., Kornei, K. A., Pettini, M., Buckley-Geer, E., Allam, S. S., & Tucker, D. L. 2009, ApJ, 701, 52
Harrison, C. M., Alexander, D. M., Mullaney, J. R., et al. 2012, ApJ, 760, L15
Hasinger, G., Miyaji, T., & Schmidt, M. 2005, A&A, 441, 417
Heckman, T. M., Kauffmann, G., Brinchmann, J., et al. 2004, ApJ, 613, 109
Henry, A., Scarlata, C., Domínguez, A., et al. 2013, ApJ, 776, L27
Hickox, R. C., Jones, C., Forman, W. R., et al. 2009, ApJ, 696, 891
Ilbert, O., McCracken, H. J., Le Fèvre, O., et al. 2013, A&A, 556, A55
Jones, T., Ellis, R. S., Richard, J., & Jullo, E. 2013, ApJ, 765, 48
Jones, T. M., Kriek, M., van Dokkum, P. G., et al. 2014, ApJ, 783, 25
Juneau, S., Dickinson, M., Alexander, D. M., & Salim, S. 2011, ApJ, 736, 104
Juneau, S., et al. 2013, ApJ, 764, 176
—. 2014, ApJ, 788, 88
Karim, A., Schinnerer, E., Martínez-Sansigre, A., et al. 2011, ApJ, 730, 61
Kauffmann, G., & Heckman, T. M. 2009, MNRAS, 397, 135
Kauffmann, G., et al. 2003, MNRAS, 346, 1055
Kelly, B. C., & Shen, Y. 2013, ApJ, 764, 45
Kewley, L. J., Dopita, M. A., Leitherer, C., et al. 2013a, ApJ, 774, 100
Kewley, L. J., Dopita, M. A., Sutherland, R. S., Heisler, C. A., & Trevena, J. 2001, ApJ, 556, 121
Kewley, L. J., Groves, B., Kauffmann, G., & Heckman, T. 2006, MNRAS, 372, 961
Kewley, L. J., Maier, C., Yabe, K., et al. 2013b, ApJ, 774, L10
Kocevski, D. D., Faber, S. M., Mozena, M., et al. 2012, ApJ, 744, 148
Koekemoer, A. M., Faber, S. M., Ferguson, H. C., & othrs. 2011, ApJS, 197, 36
Kraft, R. P., Burrows, D. N., & Nousek, J. A. 1991, ApJ, 374, 344
Kriek, M., Shapley, A. E., Reddy, N. A., Siana, B., Coil, A. L., et al. 2014, ArXiv 1412.1835
Kriek, M., van Dokkum, P. G., Franx, M., et al. 2007, ApJ, 669, 776
—. 2008, ApJ, 677, 219
Kriek, M., van Dokkum, P. G., Labbé, I., Franx, M., Illingworth, G. D., Marchesini, D., & Quadri, R. F. 2009, ApJ, 700, 221
Lacy, M., Storrie-Lombardi, L. J., Sajina, A., et al. 2004, ApJS, 154, 166
Laird, E. S., et al. 2009, ApJS, 180, 102
Liu, X., Shapley, A. E., Coil, A. L., Brinchmann, J., & Ma, C.-P. 2008, ApJ, 678, 758
Luo, B., et al. 2010, ApJS, 187, 560
Masters, D., et al. 2014, ApJ, 785, 153
McLean, I. S., Steidel, C. C., Epps, H. W., et al. 2012, in Society of Photo-Optical Instrumentation Engineers (SPIE) Conference Series, Vol. 8446, Society of Photo-Optical Instrumentation Engineers (SPIE) Conference Series
Meléndez, M., Heckman, T. M., Martínez-Paredes, M., Kraemer, S. B., & Mendoza, C. 2014, MNRAS, 443, 1358
Mendez, A. J., et al. 2013, ApJ, 770, 40
Merloni, A. 2004, MNRAS, 353, 1035
Messias, H., Afonso, J., Salvato, M., Mobasher, B., & Hopkins, A. M. 2012, ApJ, 754, 120
Moustakas, J., et al. 2013, ApJ, 767, 50
Mullaney, J. R., Pannella, M., Daddi, E., et al. 2012, MNRAS, 419, 95
Muzzin, A., Marchesini, D., Stefanon, M., et al. 2013, ApJ, 777, 18
Newman, S. F., Buschkamp, P., Genzel, R., et al. 2014, ApJ, 781, 21
Pannella, M., Carilli, C. L., Daddi, E., et al. 2009, ApJ, 698, L116
Polletta, M. d. C., Wilkes, B. J., Siana, B., et al. 2006, ApJ, 642, 673
Price, S. H., Kriek, M., Brammer, G. B., et al. 2014, ApJ, 788, 86
Rieke, G. H., & Lebofsky, M. J. 1981, ApJ, 250, 87
Rosario, D. J., Mozena, M., Wuyts, S., et al. 2013, ApJ, 763, 59
Ross, N. P., McGreer, I. D., White, M., et al. 2013, ApJ, 773, 14
Rovilos, E., Comastri, A., Gilli, R., et al. 2012, A&A, 546, A58
Salim, S., Rich, R. M., Charlot, S., et al. 2007, ApJS, 173, 267
Sanders, D. B., et al. 2007, ApJS, 172, 86
Sanders, R. L., et al. 2014, ArXiv 1408.2521
Santini, P., Rosario, D. J., Shao, L., et al. 2012, A&A, 540, A109
Shapley, A. E., Coil, A. L., Ma, C.-P., & Bundy, K. 2005, ApJ, 635, 1006
Shapley, A. E., et al. 2014, ArXiv 1409.7071
Silverman, J. D., et al. 2008, ApJ, 679, 118
Skelton, R. E., et al. 2014, ApJS, 214, 24
Stasińska, G., Cid Fernandes, R., Mateus, A., Sodré, L., & Asari, N. V. 2006, MNRAS, 371, 972
Steidel, C. C., et al. 2014, ApJ, 795, 165
Stern, D., Eisenhardt, P., Gorjian, V., et al. 2005, ApJ, 631, 163
Stern, J., & Laor, A. 2013, MNRAS, 431, 836
Tremonti, C. A., Heckman, T. M., Kauffmann, G., et al. 2004, ApJ, 613, 898
Trump, J. R., Weiner, B. J., Scarlata, C., et al. 2011, ApJ, 743, 144
Trump, J. R., et al. 2013, ApJ, 763, L6
Ueda, Y., Akiyama, M., Hasinger, G., Miyaji, T., & Watson, M. G. 2014, ApJ, 786, 104
Ueda, Y., Akiyama, M., Ohta, K., & Miyaji, T. 2003, ApJ, 598, 886
Veilleux, S., & Osterbrock, D. E. 1987, ApJS, 63, 295
Whitaker, K. E., van Dokkum, P. G., Brammer, G., & Franx, M. 2012, ApJ, 754, L29
Wright, S. A., Larkin, J. E., Graham, J. R., & Ma, C.-P. 2010, ApJ, 711, 1291
Xue, Y. Q., Brandt, W. N., Luo, B., et al. 2010, ApJ, 720, 368
Yabe, K., et al. 2012, PASJ, 64, 60
Yan, R., Ho, L. C., Newman, J. A., et al. 2011, ApJ, 728, 38
Yan, R., Newman, J. A., Faber, S. M., et al. 2006, ApJ, 648, 281